






The role of PHOX2B-derived astrocytes in chemosensory control of breathing and sleep homeostasis

Catherine M. Czeisler¹, Talita M. Silva², Summer R. Fair¹, Jillian Liu¹, Srinivasan Tupal¹, Behiye Kaya¹, Aaron Cowgill¹, Salil Mahajan¹, Phelipe E. Silva², Yangyang Wang^{3,5}, Angela R. Blissett⁴, Mustafa Göksel¹, Jeremy C. Borniger³, Ning Zhang⁹, Silvio A. Fernandes-Junior^{6,7}, Fay Catacutan¹, Michele J. Alves¹, Randy J. Nelson⁹ , Vishnu Sundaresean¹, Jens Rekling⁸ , Ana C. Takakura⁷ , Thiago S. Moreira²  and José J. Otero¹ 

¹Department of Pathology, The Ohio State University College of Medicine, Columbus, OH, USA

²Department of Physiology and Biophysics, Institute of Biomedical Science, University of Sao Paulo, Sao Paulo, Brazil

³Department of Neuroscience, The Ohio State University College of Medicine, Columbus, OH, USA

⁴Department of Mechanical and Aerospace Engineering, The Ohio State University College of Engineering, Columbus, OH, USA

⁵The Ohio State University Mathematical Biosciences Institute, Columbus, OH, USA

⁶The Ohio State University Campus Microscopy and Imaging Facility, Columbus, OH, USA

⁷Department of Pharmacology, Institute of Biomedical Science, University of São Paulo, Sao Paulo, Brazil

⁸Department of Neuroscience, University of Copenhagen, Copenhagen, Denmark

⁹Department of Neuroscience, West Virginia University, WV, USA

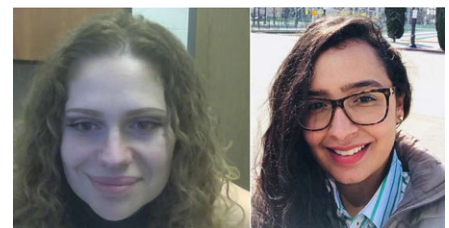
Edited by: Harold Schultz & Gregory Funk

Key points

- The embryonic PHOX2B-progenitor domain generates neuronal and glial cells which together are involved in chemosensory control of breathing and sleep homeostasis.
- Ablating PHOX2B-derived astrocytes significantly contributes to secondary hypoxic respiratory depression as well as abnormalities in sleep homeostasis.
- PHOX2B-derived astrocyte ablation results in axonal pathologies in the retrotrapezoid nucleus.

Abstract We identify in mice a population of ~800 retrotrapezoid nucleus (RTN) astrocytes derived from *PHOX2B*-positive, *OLIG3*-negative progenitor cells, that interact with *PHOX2B*-expressing RTN chemosensory neurons. *PHOX2B*-derived astrocyte ablation during early life results in adult-onset O₂ chemoreflex deficiency. These animals also display changes in sleep homeostasis, including fragmented sleep and disturbances in delta power after sleep deprivation, all without observable changes in anxiety or social behaviours. Ultrastructural evaluation of the RTN demonstrates that *PHOX2B*-derived astrocyte ablation results in features characteristic of degenerative neuro-axonal dystrophy, including abnormally dilated axon

Catherine Miriam Czeisler is an assistant professor in the department of pathology at the Ohio State University Columbus, OH where she specializes in astrocyte development and plasticity. Her research interests include the interaction between microglia and astrocytes during neuroinflammation, as well as the developmental aetiology of astrocytes in the brainstem. **Talita de Melo e Silva** received her PhD in Physiology at University of São Paulo in 2016. Currently she works as a postdoctoral researcher in the Department of Physiology and Biophysics at the University of São Paulo, Brazil. In addition, she is currently on a postdoctoral research fellowship at The Ohio State University College of Medicine. Her career is focused on neural control of autonomic systems and she is continuing to investigate how glia are involved in these functions.



C. M. Czeisler and T. M. Silva contributed equally to this work.

terminals and increased amounts of synapses containing autophagic vacuoles/phagosomes. We conclude that *PHOX2B*-derived astrocytes are necessary for maintaining a functional O₂ chemosensory reflex in the adult, modulate sleep homeostasis, and are key regulators of synaptic integrity in the RTN region, which is necessary for the chemosensory control of breathing. These data also highlight how defects in embryonic development may manifest as neurodegenerative pathology in an adult.

(Resubmitted 23 November 2018; accepted after revision 28 January 2019; first published online 1 February 2019)

Corresponding authors José J. Otero: The Ohio State University College of Medicine, Department of Pathology, 4169 Graves Hall, 333 W 10th Avenue, Columbus, OH 43210. Email: jose.otero@osumc.edu; Thiago S. Moreira, DDS, Ph.D. Associate Professor, Department of Physiology and Biophysics, Institute of Biomedical Science, University of Sao Paulo, 1524 Prof. Lineu Prestes Avenue, Sao Paulo, SP, 05508, Brazil. Email: tmoreira@icb.usp.br

Introduction

During embryogenesis, organs derive from minute embryological anlagen. These embryological anlagen give rise to all of the organ's cell types. However, it is unclear if key brainstem circuits could develop by similar principles. Proper brain development requires the generation of synaptic circuits between neurons from different central nervous system (CNS) progenitor pools, as well as glia that are needed for appropriate function of the neuronal circuit. The developmental interdependencies between astrocytes and neurons derived from similar CNS progenitor pools have been poorly explored. Given the role that glia play in the modulation of neuronal function, the interactions that developmentally linked neurons and glia may have with each other represent timely questions in developmental neurobiology. In this scenario, the present study further investigates the potential existence of developmental anlagen for neural-glia circuits implicated in CNS control of breathing and sleep homeostasis.

The paired-like homeodomain transcription factor *PHOX2B* is a major regulator of autonomic nervous system development and function. In mice, by embryonic day 9 (E9), well-demarcated zones of *PHOX2B* expression can be identified in whole mount preparations, with marked expression in rhombomere 4 (r4) and, to a lesser extent, in r2 (Pattyn *et al.* 1997). Within r4, *PHOX2B* is expressed in three progenitor domains: dA3 (characterized by *OLIG3*-positive, *PHOX2B*-positive, *TLX3*-positive and *Lmx1b*-positive cells), dB2 (characterized by *Lbx1*-positive, *PHOX2B*-positive cells), and pMNv (characterized by *PHOX2B*-positive, *NKX2.2*-positive cells). Cross-sections of the E10.5 r4 pMNv demonstrates *PHOX2B* expression in both the proliferating cells of the ventricular zone as well as the post-mitotic neurons of the mantle zone layers, where *PHOX2B* is required for appropriate neuroepithelial cytoarchitectural organization in addition to its role in neuronal specification (Dubreuil *et al.* 2000). *PHOX2B*-derived neuron specification has garnered much attention and has been extensively studied and reviewed in the scientific literature (Dubreuil *et al.* 2000; Brunet & Pattyn,

2002; Dauger *et al.* 2003). In addition to contributing to hindbrain noradrenergic (Pattyn *et al.* 2000a) and motor neuron development (Pattyn *et al.* 2000b), *PHOX2B*-expressing neurons located in the rostral aspect of the ventral lateral medulla are necessary for CO₂ detection and the hypercapnic ventilatory response (HCVR) (Stornetta *et al.* 2006; Takakura *et al.* 2008, 2014; Marina *et al.* 2010; Ramanantsoa *et al.* 2011; Ruffault *et al.* 2015). Mutation in exon 3 of *PHOX2B* causes congenital central hypoventilation syndrome (CCHS) (Amiel *et al.* 2003; Weese-Mayer & Berry-Kravis, 2004), a rare genetic disorder characterized by deficient CO₂ and O₂ detection that is worse during sleep. In humans, CCHS is characterized by loss of neurons known to be derived from the *PHOX2B* progenitor domains (Nobuta *et al.* 2015). Ventricular zone cells are *SOX2*-positive multipotent stem/progenitor cells (Peretz *et al.* 2016), and therefore *PHOX2B* expression in the hindbrain ventricular zone raises the possibility that *PHOX2B*-biased neural stem cells are also capable of forming glia. The existence of chemosensitive astrocytes (Gourine *et al.* 2010) and *PHOX2B*-derived neurons in the same anatomical area, as well as the well-documented sleep disordered breathing in patients harbouring *PHOX2B* mutations (Weese-Mayer *et al.* 2010), supports the idea that these cells and functions are developmentally linked. Therefore, in the present study we asked whether a *PHOX2B*-derived neuronal-glia unit would be involved in the regulation of the chemosensory control of breathing and sleep homeostasis.

Methods

Animal husbandry and genotyping

Animal use was in accordance with the NIH *Guide for the Care and Use of Laboratory Animals* and was approved by The Ohio State University (Protocol number 2012A00000162-R2) and University of Sao Paulo (Protocol number CEUA/ICB: 112/2015) Institutional Animal Care and Use Committee. Animals were housed under a standard 12 h light/dark cycle with *ad libitum* access to food and water. All killing guidelines

set forth by the institutional animal care and use committees were followed. The mice were sourced as follows: *ALDH1L1^{GFP-stop-DTA}* mice were provided by Dr David Rowitch (UCSF), CD1 animals utilized for astrocyte cell culture experiments were obtained from Charles River Laboratory (Cleveland, OH, USA), *NKX2.2^{cre}* mice were obtained from Dr Michael Matise (Rutgers University), *OLIG3^{cre}* mice were obtained from Dr Yahushi Nakagawa (University of Minnesota), and all other transgenic animals were obtained from Jackson Laboratories (Sacramento, CA, USA), with the following stock numbers: *Rosa^{mtdTomato/mGFP}*, Stock Number 007676; *PHOX2B^{cre}*, Stock Number 016223; *ROSA^{GZ}*, Stock Number 8606; *Rosa^{tdTomato}*, Stock Number 7908; *ALDH1L1^{cre}*, Stock Number 023748; *PHOX2B^{flp}*, Stock Number 22407; Intersectional Lineage Tracer (RC::FLTG), Stock Number 26932. Genotyping primers are delineated in the Key resources subsection in Supporting information. Briefly, tail DNA was extracted and genotyped by PCR. Primers are located in Table S1 in Supporting information.

Cell culture

Mouse embryonic stem cells (both control and *Nestin^{PHOX2B}*) were a kind gift of Lia Panman and are described in Panman *et al.* (2011) and the references therein. Cells were cultured in an undifferentiated state in Dubelco's Modified Eagle Medium (DMEM) containing 20% Fetal Bovine Serum (FBS), 100 U/ml Penicillin, 0.1 mg/ml Streptomycin, 2 mM L-Glutamine and 1000 U/ml recombinant leukemia inhibitory factor (LIF) and were induced to the neural lineage with retinoic acid as described previously (Otero *et al.* 2004b).

Whole-body plethysmography and chemoreflex analysis in conscious mice

Breathing patterns were measured in conscious mice using barometric, unrestrained whole-body plethysmography in two different laboratories located at distinct elevations and with different plethysmography systems (in São Paulo, SP, Brazil, the elevation is ~760 m, data captured by ADInstruments; in Columbus, OH, USA, the elevation is ~275 m, data captured by DSI Buxco system and Finepoint Software). Mice were acclimatized to the plethysmography chambers 2–3 days prior to the experiments. On the experimental day, freely moving mice were kept in a 500-ml plethysmography chamber with room air for 45–60 min before the ventilatory parameters were recorded. Respiratory rate (f_R , breaths min^{-1}) and tidal volume (V_T , ml kg^{-1}) were measured by whole-body plethysmography as described in detail previously (Bartlett & Tenney, 1970; Malan, 1973; Takakura *et al.* 2014). All experiments were performed at room

temperature (24–26°C). The mice were placed in a Plexiglass recording chamber (500 ml) that was flushed continuously with a mixture of 79% nitrogen and 21% oxygen (normoxia) at a rate of 0.1 l/min. During breathing measurements, the flow was interrupted and the chamber was closed for 2 min after each challenge of normoxia, hypoxia or hypercapnia.

The hypoxic ventilatory response (HVR) was induced by lowering the O_2 concentration in the inspired air to a level of 8% for 10 min. The hypercapnic ventilatory response (HCVR) was induced by titrating CO_2 into the respiratory mixture up to a level of 7% for 10 min. The pressure oscillations caused by breathing were monitored using a differential pressure transducer (ML 141 Spirometer, ADInstruments) and the pressure signal was amplified, filtered, recorded, and analysed off-line using Powerlab software (Powerlab 16/30, ADInstruments, NSW, Australia). Rectal temperature was measured before and at the end of the experiments, and the values were averaged. Changes in the f_R , V_T and minute ventilation (\dot{V}_E) ($f_R \times V_T$; ml $\text{min}^{-1} \text{kg}^{-1}$) were averaged and expressed as means \pm SEM. The hyperoxic hypercapnic response was performed in the DSI Buxco system using the following protocol: 20 min baseline room air, 3 min hyperoxia (65% O_2 , balanced, N_2), hyperoxic hypercapnia (65% O_2 , 7% CO_2 , balanced N_2), and 20 min recovery in room air.

Physiological experiments under sleep state

Transmitter implantation and biopotential recording. Mice were deeply anaesthetized under isoflurane (3% induction, 1.5% maintenance) and implanted with PhysioTel F20-EET (Data Sciences International [DSI], St Paul, MN, USA) biotelemetry units to allow acquisition of electroencephalogram (EEG) and electromyogram (EMG) potentials as described previously (Borniger *et al.* 2018). Following immobilization in a stereotaxic apparatus, a midline incision was made between the posterior margin of the eyes and the midpoint of the scapulae. The skull was exposed and cleaned, and two stainless steel screws (00-96 \times 1/16; Plastics One, Roanoke VA, USA) were inserted through the skull to make contact with the underlying dura mater. These screws served as cortical electrodes. One screw was placed 1 mm lateral to the sagittal suture and 1 mm anterior to bregma. The other screw was placed contralaterally 2 mm from the sagittal suture and 2 mm posterior to bregma. The transmitter itself was inserted into a subcutaneous pocket along the back of the animal. A set of leads was attached to the cortical electrodes and secured with dental cement. Another set of leads was inserted into the trapezius muscles for EMG measurement. The surgical procedures were performed using aseptic technique, and buprenorphine (0.05 mg/kg, s.c.) was administered to provide post-operative analgesia along with supplemental

warmth (heating pad) until the animals were mobile. Following surgery, mice were singly housed and their cages were placed on top of receiver boards (RPC-1; DSI) in ventilated cabinets. These boards relay telemetered data to a data exchange matrix (DSI) and a computer running Ponemah software (version 6.1; DSI). Mice were allowed to recover from the surgery for 2 weeks prior to beginning 2 days of baseline sleep recording.

Sleep deprivation. Following baseline recordings, a sleep deprivation protocol was performed to examine the homeostatic response to sleep deprivation. Total sleep deprivation was accomplished via 'gentle handling' during the first 6 h of the rest phase (ZT 0–6), followed by an 18 h recovery period (as described in Oyanedel *et al.* 2015). If EEG/EMG biopotentials showed signs of sleep and the animal displayed a sleeping posture, then the cage was gently tapped to arouse the mouse. If this did not prevent sleep, then the experimenter would briefly handle the mouse or disrupt its bedding. As this method is dependent on live monitoring of EEG/EMG and sleep posture, this method cannot eliminate all sleep, and small episodes (< 10s) of 'micro-sleeps' persisted.

Sleep architecture and spectral analyses. Raw biopotentials were band-passed (0.3–25 Hz for EEG and 25–50 Hz for EMG) and analysed in 10 s epochs via the automated rodent sleep scoring module in Neuroscore (DSI) as previously described (Borniger *et al.* 2018). Delta and theta ratio criteria, as well as EMG threshold values (for scoring of NREM, REM and wake, respectively), were adjusted on a per-animal basis to ensure accurate scoring across the experimental set. Delta band was set at 0.5–4.0 Hz, and the theta band was set at 6.0–9.0 Hz. Artifact detection thresholds were set at 0.4 mV for both EMG and EEG, and if an epoch > 10% fell outside this threshold, the entire epoch was scored as artifact. Wake was characterized by high frequency and low voltage EEG accompanied by high voltage EMG. NREM (i.e. slow wave sleep) sleep was characterized by low frequency and high voltage EEG (predominant delta), accompanied by low voltage EMG. REM (i.e. paradoxical) sleep was characterized by low voltage EEG (predominant theta) and EMG values. Ten-second epochs were collapsed into 2 h bins for subsequent graphing and statistical analyses. The percentage time spent in each vigilance state was calculated across a recording period (light or dark phase), as well as the number of vigilance state transitions (and directionality of these transitions) and the duration of each bout in each vigilance state as a measure of sleep fragmentation.

For spectral analyses, biopotentials were visually inspected, cleaned of artifacts, and subjected to fast Fourier transforms. Periodogram data were collected in 10 s

epochs covering the entire baseline recording period and 0–6 h post-sleep deprivation. Vigilance state spectra were generated across a frequency range of 0.49–23.97 Hz (sampling rate of 500 Hz).

Histology and microscopy

Confocal immunofluorescence. Animals were killed and perfused with 4% paraformaldehyde. The brains were dissected and then underwent post-perfusion fixation overnight at 4°C in 4% paraformaldehyde-PBS. Brains were then transferred to 30% sucrose (w/v)-PBS and allowed to equilibrate prior to embedding in OCT. Cryosections were then either mounted on glass slides or placed into 24-well dishes and stained using antibodies. Cryosection thicknesses ranged from 12 μm to 40 μm , depending on application. Prolong-gold Antifade kit was utilized for mounting on glass coverslips. Images were captured as black and white images on an LSM 700 Zeiss Confocal Microscope. Images were saved as .czi files, opened in FIJI to be saved as .tiff files, and then imported to Adobe Photoshop for pseudocolouring as needed. All figures were prepared using Adobe Illustrator.

Histochemistry and immunohistochemistry. For experiments requiring X-gal histochemistry, the animal was transcardially perfused with PBS, followed by 4% paraformaldehyde. The brain was dissected out and incubated in 4% paraformaldehyde for 1 h on ice and then washed with PBS. The brains were cryoprotected by incubation with 30% sucrose in PBS overnight and embedded in OCT for cryosectioning. Cryosections 50 μm thick were collected in each well of a 48-well plate pre-filled with PBS. The floating sections were washed three times for 15 min with solution C (2 mM magnesium chloride, 0.02% Igepal (Sigma-Aldrich, St Louis, MO, USA; 13021), 0.01% sodium deoxycholate (Sigma-Aldrich D5670), 5 mM EGTA (Sigma-Aldrich E4378)). The sections were then incubated with staining solution (solution C containing 10 mM potassium hexacyanoferrate (III) (Sigma-Aldrich P8131), 10 mM potassium hexacyanoferrate (II) trihydrate (Sigma-Aldrich P3289) and 0.5 mg/ml X-GAL (Roche Diagnostics GmbH, Mannheim, Germany; 651745)). The floating sections were incubated in this solution in the 48-well plate overnight at room temperature in the dark. The next day, the tissue sections were washed with PBS and mounted on a slide previously coated with Vectabond (Vector Labs SP-1800) using a fine paintbrush. The sections were allowed to dry on the slide for 30 min at room temperature and then counterstained with a 30-min incubation with Haematoxylin (without the blueing step to aide in contrasting the X-gal with cell nuclei) and mounted with Vectamount (Vector Labs H-5000). For chromogenic immunohistochemical reactions using

PHOX2B and tyrosine hydroxylase antibodies (TH), the following protocols were used. The brains were sectioned in the coronal plane at 30 μm on a microtome and stored in cryoprotectant solution (20% glycerol plus 30% ethylene glycol in 50 mM phosphate buffer, pH 7.4) at -20°C . The locations of immunoreactive TH and Phox2b in the commissural NTS (-7.48 to -8.12), C1 (-6.48 to -7.08) and RTN (-5.68 to -6.48) were analysed in one section in each 180 μm relative to bregma. Phox2b was detected using a polyclonal anti-Phox2b raised in rabbit (1:800 dilution; gift from J.-F. Brunet, Ecole Normale Supérieure, Paris, France). TH was detected using a mouse antibody anti-TH (MAB 318; Millipore; dilution 1:1000). Sections were incubated for 24 h at room temperature and diluted in PB containing 10% normal horse serum (008-000-001; Jackson Immuno Research Laboratories) and 0.3% Triton X-100. After several rinses, they were transferred to the appropriate affinity purified biotinylated secondary antibodies (donkey anti rabbit (BA-1000, Vector, dilution 1:500) for Phox2b and donkey anti-mouse (715-065-151, Jackson Immuno Research Laboratories, dilution 1:500) for TH), all diluted in PB containing 1% normal horse serum and 0.3% Triton X-100, incubated for 24 h at room temperature, rinsed again and exposed to Extravidin (E2886; Sigma-Aldrich; dilution 1:2000) for 4 h at room temperature. Peroxidase reactions were visualized using the glucose oxidase procedure and 3,3'-diaminobenzidine (DAB) tetrahydrochloride as chromogen for TH and associated with 0.5% nickel sulfate for Phox2b immunostaining. Sections were rinsed again in PB, mounted in sequential rostrocaudal order onto gelatin-coated slides, dehydrated through a series of ascending concentrations of ethanol, transferred into xylene, and coverslipped with DPX (06522; Sigma Aldrich) mountant for histology.

Unbiased stereology. All unbiased stereology was performed on Stereoinvestigator from MBF Biosciences. For unbiased stereological quantification, parameters were as follows: dissector height (Z) = 20 μm , dissector volume = 50,000 μm^3 , guard zone distance setting = 10 μm , section evaluation interval = 2. For unbiased stereological quantification of PHOX2B-positive cells, 50 μm sections of the RTN region were stained using DAKO Envision kit or LSAB universal kit, followed by Haematoxylin counterstaining. A Zeiss Axioimager A1 microscope (Zeiss, Muenchen, Germany) was used to image sections and perform subsequent analysis. The profile counts of labelled cells reflected the average of the bilateral side of the medulla. Digital colour photomicrographs were acquired using a Zeiss AxioCam HRC camera.

Electron microscopy. Animals were perfusion-fixed with 4% paraformaldehyde. Brains were extracted and

placed in fresh fixative, 2% paraformaldehyde, 2.5% glutaraldehyde in PBS (pH 7.2), for 2 days at 4°C . Tissue was then washed for 24 h in PBS. Brains were embedded in 4% agarose and sectioned at 300 μm thickness on a vibratome. Sections were stored in PBS and delivered to the Campus Microscopy & Imaging Facility at Ohio State University for TEM processing. All processing steps are carried out at room temperature. Samples were post-fixed in 0.1 M osmium tetroxide for 2 h, followed by thorough rinsing in distilled water and en bloc staining with 2% ethanolic uranyl acetate. Samples underwent dehydration through a graded ethanol series (30–100%) and transitioned into acetone for resin infiltration. An epoxy resin, Eponate 12 (Ted Pella) was used for a graded infiltration series and embedding. Final embedding was done in a flat embedding mould and weighted down with a pre-polymerized BEEM capsule to ensure proper orientation and avoid warping of tissue. Tissue was placed in a 60°C oven and polymerized overnight. Blocks were trimmed and semi-thin sections (500 nm) cut on a glass knife and stained with 1% Toluidine Blue stain to identify slices containing the RTN. The region of interest was further trimmed, and 70 nm thin sections were cut using a diamond knife (Diatome, Inc.) on a Leica EM UC6 ultra-microtome. Thin sections were collected on 200 mesh copper grids and post-stained with 1% uranyl acetate and Reynold's lead citrate. TEM micrographs were taken on a FEI Tecnai G2 Biotwin TEM operating at 80 kV and micrographs captured using an AMT camera. Three animals per group were evaluated in this fashion.

Astrocyte culture

Pups at postnatal days (P) 0–3 were decapitated and the ventral hindbrain was dissected out in ice-cold HBSS with $1\times$ antibiotic-antimycotic (ThermoFisher Scientific 15240096) and then each hindbrain was transferred to a 6- to 12-well plate containing 1 ml of room temperature Accutase (Stem Cell Technologies 07920). Hindbrains were mechanically dissociated with a P1000 pipette and incubated in a humidified incubator at 37°C for a total of 10 min. The cell mixtures were then passed through a 70 μm nylon filter (BD Falcon, 352350) and combined with 5 ml astrocyte medium (DMEM containing 10% FBS, 2 mM L-glutamine, 100 U/ml penicillin/streptomycin and 200 ml/ml N2 serum supplement) and centrifuged at 820g in a Beckman Coulter Allegra 6R Centrifuge for 7 min. The cell supernatants were discarded and the pellets resuspended with 5 ml of astrocyte media. The mixtures were centrifuged again, the supernatants discarded and the cell pellets were resuspended in 1 ml astrocyte medium. Astrocytes derived from each animal were separately plated in a single well of a 24-well plate on a glass coverslip previously coated with poly-L-lysine (Sigma-Aldrich P6282). The medium was changed after 24 h and then again every

3 days until the cells became confluent. Once the cells reached confluence, the plate was placed on a 225 rpm orbital shaker at 37°C overnight to dislodge non-adherent cells. The following day, the medium was changed and the cells were placed back into the incubator to recover for 48 h. After 48 h, the cells were treated with 1 mM cytosine arabinoside (AraC, Sigma Aldrich C1768) overnight and then left to recover for another 48 h. This technique yields a roughly 98% pure astrocyte culture.

Fluo-8 dye loading and calcium imaging

After the 48 h of recovery post-AraC treatment, the astrocyte cultures were subjected to dye loading and calcium imaging. Cells were incubated for 30 min in a humidified incubator at 37°C, 5% CO₂ with 2–5 mg/ml Fluo8 (Abcam ab142773) in aCSF (120 mM NaCl, 21 mM NaHCO₃, 0.58 mM NaH₂PO₄, 8 mM KCl, 1.5 mM MgCl₂, 1.26 mM CaCl₂, 30 mM glucose, equilibrated with 95% O₂ and 5% CO₂ for 20 min, and pH was adjusted to either 7.4 or 7.2 with HCl or NaOH). The cultures recovered by incubating with aCSF (pH 7.4) in a 37°C, 5% CO₂ humidified incubator for another 30 min. Coverslips were individually placed on an open bath recording chamber (RC-22C, Warner Instruments) set up with a single channel heater controller (110-230 VAC, 50/60 Hz, Harvard Apparatus) set to maintain the aCSF at 30°C in the chamber. The aCSF was perfused using gravity flow at a rate of 1 ml/min and constantly bubbled with 95% oxygen and 5% carbon dioxide. For acidification challenge, the pH 7.4 aCSF perfusates were switched to aCSF at pH 7.2 for the challenge, and then returned to aCSF at pH 7.4. During the experiments, the pH was continuously monitored to observe for pH drift, and aCSF was made fresh before each experiment. For the hypoxia challenge, aCSF was kept at pH 7.4 and was either bubbled in 95% oxygen and 5% carbon dioxide (carbogen), or bubbled in 100% nitrogen gas for 1 h prior to the experiment. It should be noted that after N₂ gas bubbling the buffer increased in pH due to precipitation of Ca(HCO₃)₂. We attempted to return the pH to 7.4 in this buffer by titrating back the pH to 7.4 after 20 min of bubbling and continued to bubble Nitrogen throughout the experiment. Perfusates were switched from aCSF-carbogen to aCSF-nitrogen gas for the hypoxia challenge, and then perfused with aCSF-carbogen for recovery. N₂ gas is commonly used to deoxygenate aCSF (Angelova *et al.* 2015).

The cells were visualized using an upright Zeiss Axioskop 2 mot *plus* microscope using a 10× air objective with an LED light source of 470 nm (Prismatix, Israel) and movies were captured using an Andor iXon Ultra CCD camera operating at 10 frames/s with an exposure time of 90 ms. Movies were captured using mmanager software (freeware) and began 2 min after the sample was placed in the bath and 2 min after the pH was changed. All

movies were taken for a duration of 3 min. Once captured, movies were subjected to analysis in Matlab (MathWorks Inc., Natick, MA, USA) to determine active regions and synchronicity. The code was written based on the software CaSCaDe (Ca²⁺ Signal Classification and Decoding) reported in Agarwal *et al.* (2017). The complete workflow was carried out as follows. First, a noise reduction was applied on each frame of the movie with the Gaussian filter of size 45*45. Next, the data were projected and averaged along the time axis. From the averaged data, local maximums of fluorescence intensity are labelled out using threshold of $\mu_{bg} + 2\sigma_{bg}$, where μ_{bg} and σ_{bg} are the mean and standard deviation of the intensity level, respectively. Then, the intensity time series from all local maximal regions are normalized after subtracting μ_{bg} , and the active regions are picked out for those having peak signals of intensity greater than 5.0 over 4 adjacent frames. Peaks from different active regions that have more than 50% overlap in time are considered as synchronized and automatically detected.

Statistical analysis

Respiratory physiology experiments in conscious mice. All custom R-scripts utilized in the proposed research are located in the Supporting information. Data were analysed by one- or two-way ANOVA with repeated measures, with differences between groups determined using Sidak multiple comparisons in the SPSS Statistics software (version 22, IBM, Armonk, NY, USA) or GraphPad Prism 5.0 (GraphPad Software, San Diego, CA, USA). Assumptions of the two-way ANOVA were tested with the Shapiro-Wilk test for normality on error residuals both between and within subjects (R statistical software package version 3.2.0; R Core Team, 2013). Assumptions of the one-way ANOVA for normality were also confirmed with the Shapiro-Wilk test. Student's *t* test was used to compare each outcome between control and experimental groups for the neurobehavioral experiments. Test statistics where $P < 0.05$ were considered significant.

Unbiased stereological quantification of astrocyte ablation and PHOX2B immunoreactive cells in the ventral lateral medulla, and serial section quantification of PHOX2B- and TH-positive cells. For each group, $n = 3$ animals were used as described previously by our group (Otero *et al.* 2014; Gokozan *et al.* 2016; Gygli *et al.* 2016). Arithmetic means for each structure were determined for control and experimental groups, and statistical hypothesis testing was performed by Student's *t* test. Serial section quantifications for PHOX2B in NTS_c, and RTN and of TH in C1 were performed in $n = 4$ animals per group (Control was $ALDH1L1^{loxP-GFP-loxP-DTA}$, experimental was $PHOX2B^{cre}$, $ALDH1L1^{loxP-GFP-loxP-DTA}$).

Sleep physiology experiments. For each group, $n = 4/\text{sex}/\text{genotype}$. Differences in sleep architecture (percentage time in each state, number of bouts, and bout durations), as well as activity over an entire baseline recording period, were analysed using repeated-measures ANOVAs with genotype and sex as independent variables. To provide time-point-specific analysis, two-tailed Student's t tests at each time point were used. A $P < 0.05$ (two-tailed) alpha was considered significant. All statistical analyses were completed with SPSS Statistics software (version 22, IBM) or GraphPad Prism 5.0 (GraphPad Software).

Neurobehavioral experiments. Anxiety testing was performed as described previously by our group (Gygli *et al.* 2016). Student's t test was used to compare each outcome between control and experimental groups.

In vitro astrocyte calcium signalling quantification. The number of active domains was determined and analysed by an automated image analysis algorithm described above. Mean active domains, fold synchronization, and fold increase in mean active domains were plotted using Rv3.4.1. Each movie was obtained from one cover slip recording per animal in the hypoxia and acidification challenge experiments. Brainstem astrocyte preparations were obtained from one animal from the following two groups: Control group is $ALDH1L1^{\text{loxP-GFP-loxP-DTA}}$; experimental group is $PHOX2B^{\text{cre}}, ALDH1L1^{\text{loxP-GFP-loxP-DTA}}$. Statistical hypothesis testing was performed by ANOVA/Tukey HSD test.

Ultrastructural morphometry analysis. Transmission electron photomicrographs were captured while the experimenter was blinded to genotype from the RTN/VLM area and morphometric analysis was performed manually using FIJI. All parameters were evaluated *post hoc*. Synaptic area and perimeter EM data were pooled for each group for statistical analysis as described previously (Hazai *et al.* 2013). For the autophagic vacuole analysis, the mean percentage of axon terminals containing autophagosomes was calculated for each animal and then averaged per group. Shapiro's test of normalcy was used to evaluate the nature of the data, followed by a Student's t test.

Results

PHOX2B biased progenitor cells generate astrocytes

In order to determine the effects of $PHOX2B$ on astrocyte differentiation, we utilized the $Nestin^{\text{Phox2B}}$ embryonic stem (ES) cell model, which expresses $PHOX2B$ under the control of the $Nestin$ promoter (Panman *et al.* 2011). ES cells were differentiated into hindbrain neurons and glia using retinoic acid (Otero *et al.* 2004a). These data are

illustrated in Fig. 1A. As expected, neuron production was accelerated in the $PHOX2B$ -expressing neural stem cells relative to controls, with robust neurofilament-positive neurites appearing 8 days after embryoid body formation. Ultimately, both groups generated extensive pools of astrocytes following retinoic acid induction 7 days post plating on matrigel, giving 15 days total differentiation (Fig. 1A–E). We conclude that $PHOX2B$ expression in ES cell-derived neural stem cells does not prevent astrocyte development in the $Nestin^{\text{Phox2B}}$ embryonic stem (ES) cell model.

To confirm these data *in vivo*, we interbred $PHOX2B^{\text{cre}}$ mice with a series of lineage tracer mice (Fig. 2 shows transgenic strategy), and performed neuroanatomical analyses (Fig. 3). Although the majority of the $PHOX2B$ -derived brainstem cells are neuronal, a significant population of astrocytes characterized by robust glial fibrillary acidic protein (GFAP) expression are located in the ventral lateral medulla in areas overlapping with the retrotrapezoid nucleus (RTN) (Fig. 3A–D). These $PHOX2B$ -derived astrocytes do not express $PHOX2B$. We verified these data using other, independent transgenic strategies. These included $PHOX2B^{\text{cre}}, ROSA^{\text{GFP}}$, which also showed GFAP-positive, green fluorescent protein (GFP)-positive astrocytes in the RTN region (Fig. 3E; see Fig. 1A for transgenic strategy). Similar findings were also seen in $PHOX2B^{\text{cre}}, ROSA^{\text{GNZ}}$ animals (Fig. 3F1; see Fig. 1E for transgenic strategy).

Next, we tested the extent to which $PHOX2B$ -derived astrocytes could be labelled using an intersectional genetic strategy, shown in Fig. 3G–I (see Fig. 1C for transgenic strategy). In these experiments, which utilize a different promoter design than the $PHOX2B^{\text{cre}}$ (Hirsch *et al.* 2013), cells expressing the astrocyte promoter $ALDH1L1$ and $PHOX2B$ show GFP expression, whereas $PHOX2B$ expression alone promotes *tdTomato* expression. We note that $PHOX2B$ -derived, $ALDH1L1$ -derived cells are morphologically consistent with astrocytes and make intimate contacts on the cell body and dendritic arborization of $PHOX2B$ -derived cells that are morphologically consistent with neurons (Fig. 3H–I). The GFP-labelled population (indicating $ALDH1L1$ -expressing $PHOX2B$ -derived cells) in these intersectional genetics experiments was smaller than the $NKX2.2^{\text{cre}}$ -derived *tdTomato*-expressing cells (Fig. 4), possibly indicating that the population of $PHOX2B$ -derived astrocytes in the RTN represents a sub-population of all of the RTN astrocytes.

We next sought to understand the possible progenitor domains that give rise to ventral medullary surface astrocytes. By using $OLIG3$ and *Rosa tdTomato* reporter mice, we noted that ventral medullary astrocytes were not derived from $OLIG3$ -expressing cells, indicating that they were not derived from the dA3 embryonic progenitor domain (Fig. 4). However, we noted a robust

appearance of ventral medullary astrocytes derived from *NKX2.2*-expressing cells, suggesting that these cells may be derived from the pMNV progenitor domain, an area characterized by overlapping and non-overlapping embryonic *PHOX2B*- and *NKX2.2*-expressing progenitor cells (Fig. 4B and B').

We also characterized *Aldh1L1* expression in developing hindbrain progenitor cells to ensure that *PHOX2B* expression preceded *ALDH1L1* expression. Our data show that *ALDH1L1* is absent from *PHOX2B* progenitor cells in the pMNV domain at E10.5 (Fig. 4C), a time point characterized by robust visceral motor neuron formation (Pattyn *et al.* 2003). We therefore conclude that the GFP cells are not the result of *ALDH1L1* expression in pMNV embryonic progenitors, but that these cells first expressed *PHOX2B* followed by *ALDH1L1* expression

at later developmental time points. The close contact observed between *PHOX2B*-derived neurons and glia taken together supports the existence of a unique neuroglial unit for autonomic function. We further deduce that these *PHOX2B*-derived RTN astrocytes are not derived from the dA3 (i.e. *OLIG3/PHOX2B* domain). Rather, these *PHOX2B*-derived astrocytes represent glia generated in the pMNV progenitor domain.

Astrocyte ablation is centred in the ventral lateral medulla

Having demonstrated *PHOX2B* derivation of RTN astrocytes and RTN neurons, we next set forth to determine the extent to which ablation of these astrocytes

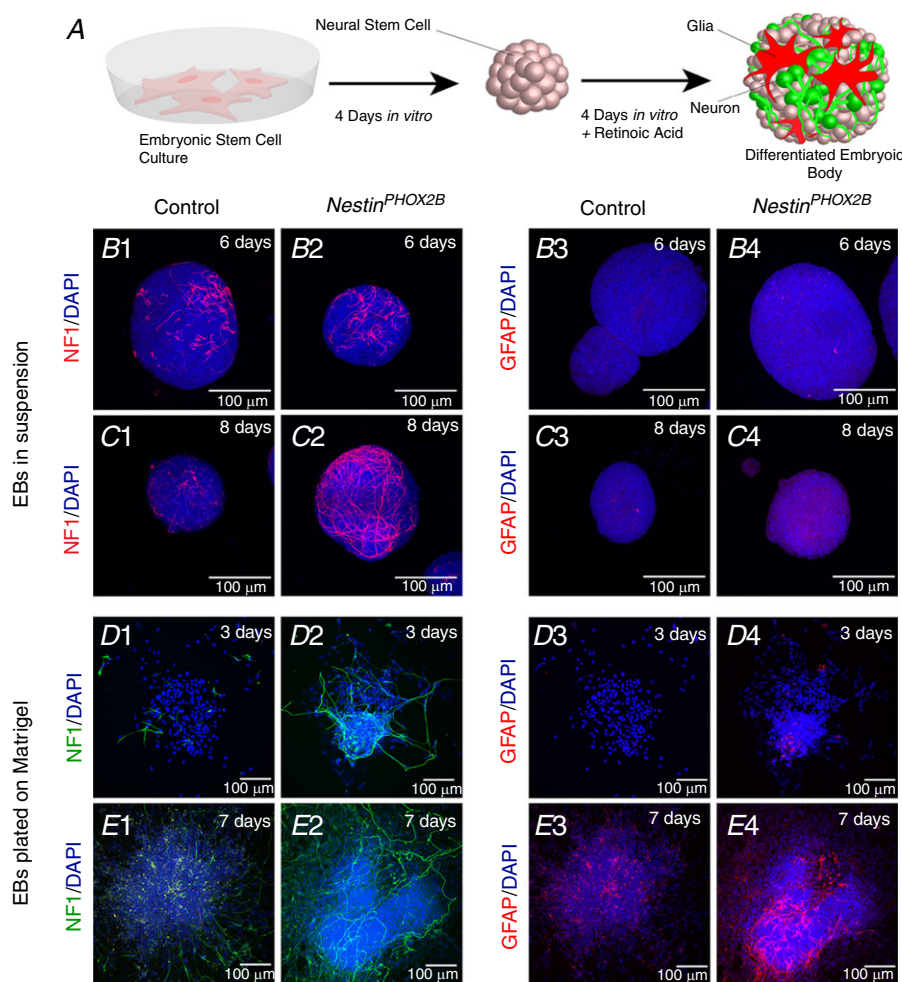


Figure 1. PHOX2B expression does not prohibit astrocyte generation

Embryonic stem cells were differentiated by dilution and retinoic acid through embryoid body formation (schematic diagram shown in A). Controls included wild-type ES cells, and experimental ES cells contain a cassette that expresses *PHOX2B* under the control of the *Nestin* promoter (*Nestin^{PHOX2B}*). B and C represent confocal optical slices of embryoid bodies that underwent immunofluorescence analysis through whole-mount staining. Molecular markers are denoted on the left-hand side of each panel. Top right indicates days of differentiation in each step (embryoid body phase in B and C and post-embryoid body dissociation and plating on matrigel in D and E). NF, neurofilament; EB, embryoid body). [Colour figure can be viewed at wileyonlinelibrary.com]

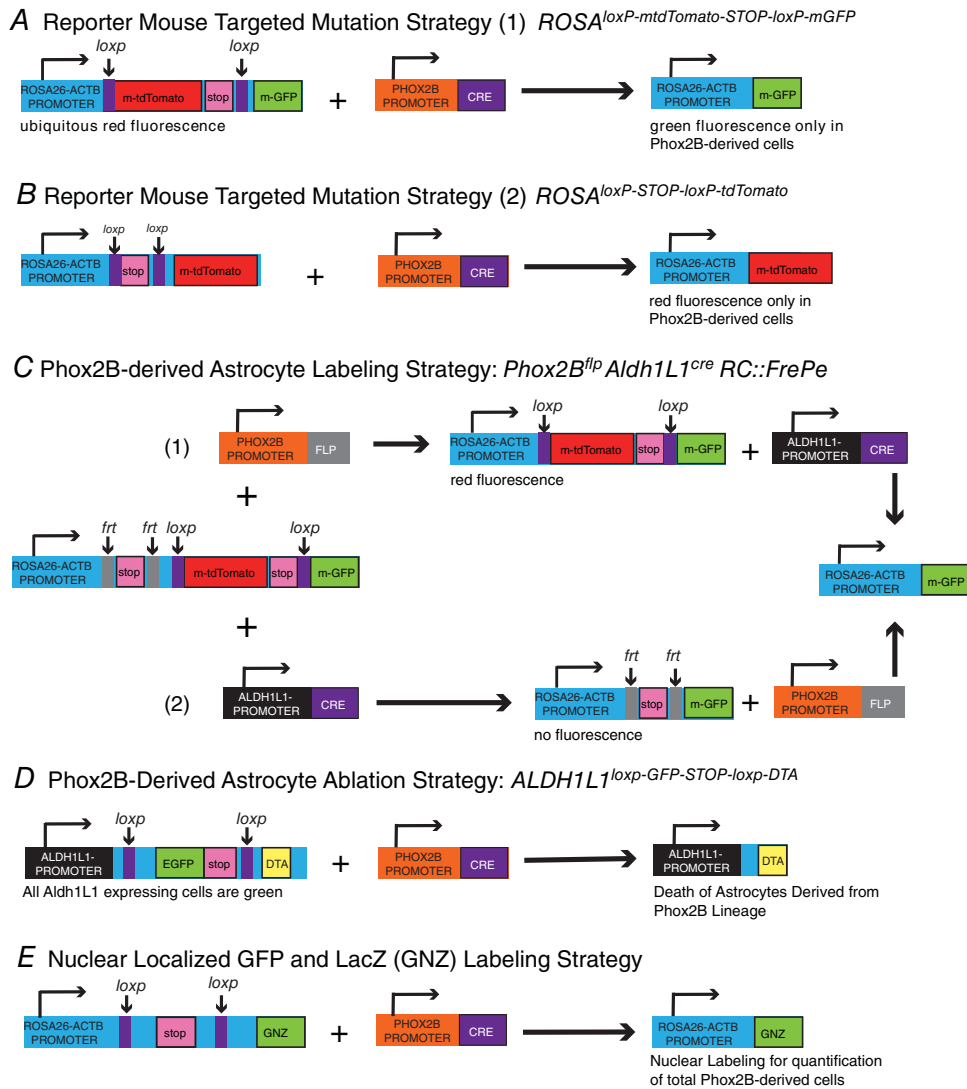


Figure 2. Graphical depiction of transgenic mouse strategies

A, several lines of transgenic mice were used to obtain lineage tracing results for *PHOX2B*-derived populations, including the *ROSA^{mtImG}*, a cell membrane-targeted, two-colour fluorescent Cre-reporter allele. When bred to *PHOX2B*-cre mice, cell membrane-localized GFP (mGFP) fluorescence expression is widespread in *PHOX2B*-expressing (cre-recombined) cells. B, the *ROSA^{loxP-STOP-loxP-tdTomato}* reporter mice harbour a loxP-flanked *STOP* cassette preventing transcription of a CAG promoter-driven red fluorescent protein variant (tdTomato). TdTomato is expressed in *PHOX2B*-derived tissues when bred to *PHOX2B*-Cre mice. C, the *RC::FrePe* dual-recombinase responsive fluorescent allele has a *frt*-flanked *STOP* and loxP-flanked mCherry::STOP all preventing transcription of eGFP. FLP recombinase (by breeding with *PHOX2B*-flp mice) results in mCherry fluorescence, and further exposure to Cre recombinase (by breeding with *ALDH1L1*-cre mice) results in eGFP fluorescence in the overlapping populations. Two recombination events are possible, namely (1) in which the *PHOX2B* promoter is first turned on, resulting in red fluorescence, followed by the *ALDH1L1* promoter, resulting in green fluorescence, or (2) which consists of *ALDH1L1* turning on first, with no resulting fluorescence, followed by *PHOX2B*, resulting in green fluorescence. D, in this *PHOX2B*-derived astrocyte ablation strategy, we used a transgenic strain where *ALDH1L1* promoter-active cells in the brain and spinal cord (the majority being astrocytes) express EGFP. Crossing with *PHOX2B*-cre mice results in Cre-mediated excision of the floxed *EGFP/Stop* enabling DTA-mediated ablation of these cells. E, for labelling single *PHOX2B*-derived cells we used GNZ knock-in mice which have widespread expression of a nuclear-localized green fluorescent protein/beta-galactosidase fusion protein (GFP-NLS-lacZ or GNZ) upstream of loxP-flanked *STOP* sequence. When bred to *PHOX2B*-cre-expressing mice, the resulting GNZ fusion protein expression in the offspring allows for enhanced (single cell level) visualization. [Colour figure can be viewed at wileyonlinelibrary.com]

affected physiological conditions. To achieve this goal, we utilized the astrocyte ablation technique described by Tsai *et al.* (2012). In this model, the astrocyte-specific *ALDH1L1* promoter induces *GFP* expression in the absence of *cre* recombinase and diphtheria toxin A (DTA) in the presence of *cre* recombinase (see Fig. 1B for transgenic strategy). We interbred these *ALDH1L1^{loxP-GFP-STOP-loxP-DTA}* mice with *PHOX2B^{cre}* mice and found that these mice were born under expected Mendelian ratios. We first sought to determine if the number of RTN *PHOX2B*-immunoreactive neurons was significantly different between these animals. To test this, we performed two independent analyses utilizing distinct *PHOX2B* antibodies, as well as distinct quantification workflows (unbiased stereology *vs.* serial

section immunohistochemical analysis). We did not find a significant difference in total *PHOX2B*-positive neuron number nor in *PHOX2B*-positive rostral-caudal distribution of RTN neurons (Fig. 5A1–3, C1–3). We also did not find any differences in the catecholaminergic C1 *PHOX2B*-positive/TH-positive neurons between groups, nor in commissural NTS *PHOX2B*-positive cells (Fig. 5D1–E3). We conclude that DTA expression in *PHOX2B*-derived, *ALDH1L1*-expressing cells does not alter the generation of *PHOX2B*-positive neurons in these regions.

Upon evaluation of the RTN region, we did not observe an appreciable decrease in GFAP-positive or *ALDH1L1*-positive cells. Objective quantification of astrocytes is fraught with caveats (Ostergaard & Jensen,

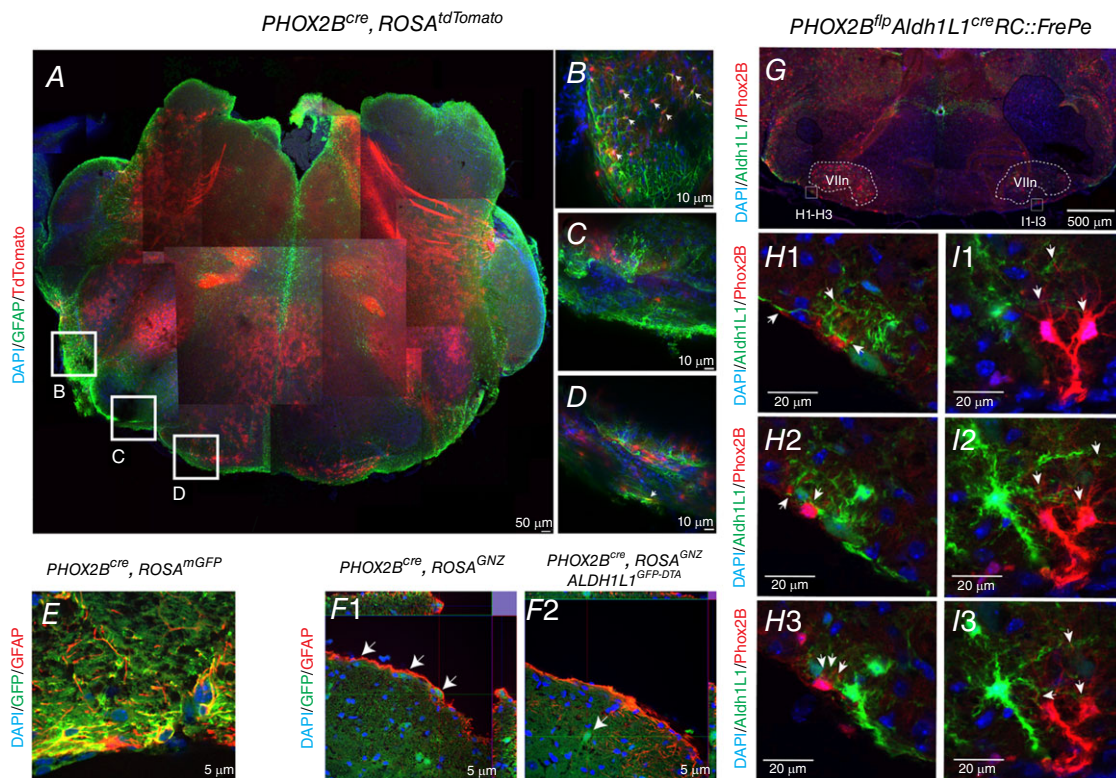


Figure 3. *PHOX2B*-derived astrocytes identified *in vivo*

Genotypes are on the top of each panel series, and molecular markers are illustrated on the left. A shows a low magnification, optically cleared specimen stained with GFAP (green) and showing endogenous tdTomato expression that was manually tiled. B–D are higher magnification images of this specimen, illustrating a small quantity of *PHOX2B*-derived astrocytes located on the ventral medullary surface. E, a photomicrograph captured from the RTN region of an animal showing post-*cre*-mediated, constitutive expression of a membrane-tethered GFP protein (green); the sections were also stained with GFAP (pseudo-coloured in red) showing *PHOX2B*-derived astrocytes in yellow. F1, *cre*-mediated recombination induces expression of GFP fused to β -galactosidase. Note the GFP-positive astrocyte on the edge of the medullary surface. F2, ablation of *PHOX2B*-derived astrocytes does not abrogate expression of *PHOX2B*-derived neurons (F2, arrow) yet removes the *PHOX2B*-derived astrocytes from the medullary surface. G, low power view of an intersectional transgenic mouse experiment, which results in tdTomato expression following flp-mediated recombination, and GFP expression following recombination by both flp- and *cre*-recombinase. Flp was under the *PHOX2B* promoter, whereas the astrocyte marker *ALDH1L1* controls *cre*-expression. *PHOX2B*-derived/*ALDH1L1*-derived cells are labelled in green. Two high magnification confocal slice series are shown in H1–I3, and show intimate associations between *PHOX2B*-derived/*ALDH1L1*-derived cells and *PHOX2B*-derived cells. [Colour figure can be viewed at wileyonlinelibrary.com]

2013), especially in the RTN region where, unlike in the cerebrum (Bushong *et al.* 2002; Ogata & Kosaka, 2002), astrocytes show highly overlapping domains (Sheikhabahaei *et al.* 2018). These highly overlapping RTN astrocyte domains preclude objective and accurate quantification by cytoplasmic glial markers. We were therefore obligated to validate the extent of glial ablation through genetic methodologies. This was made possible by taking advantage of the *ROSA^{GNZ}* transgenic mouse, which expresses *beta-galactosidase* in cells after *cre*-mediated recombination (see graphical depiction in Fig. 1E). In both experimental and control groups, *PHOX2B^{cre}*-derived cells express GFP fused to *beta-galactosidase*, and therefore show X-gal positivity. Unbiased stereological quantification of X-gal-positive cells in the RTN region yielded a significant difference of ~800 fewer cells in the experimental mice, with 400–600 X-gal-positive cells remaining in the experimental animals (Fig. 5B1–3), a value approximating the total number of RTN *PHOX2B*-positive neurons (Fig. 5A3 and C3).

Cytoarchitectural analysis of the ventrolateral medulla was performed by confocal microscopic analysis of brainstem sections stained with GFAP, *PHOX2B*, ISLET1, tyrosine hydroxylase (TH), tryptophan hydroxylase (TrpOH), galanin, and NK1R antibodies (Fig. 5F–I and Fig. S1 in Supporting information). The ventrolateral medulla (VLM) did not demonstrate any overt defects in astrocyte quantity, astrocyte morphology and cytoarchitecture, RTN neurons, facial nucleus (VII) neuron morphology, or neurochemical composition of VLM neurites (Fig. 5F–I). Although brainstem astrocytes show distinct morphologies to cortical astrocytes (Sheikhabahaei *et al.* 2018), thus making the definition of brainstem gliosis challenging, we did not find an increase in astrocyte number or morphologies in the *PHOX2B*-astrocyte-ablated mice in the RTN region. We also tested the extent to which *PHOX2B*-astrocyte ablation resulted in changes in the number of *PHOX2B*-derived cells in the locus coeruleus, dorsal motor nucleus of the vagus nerve, and VII nucleus, all of which are

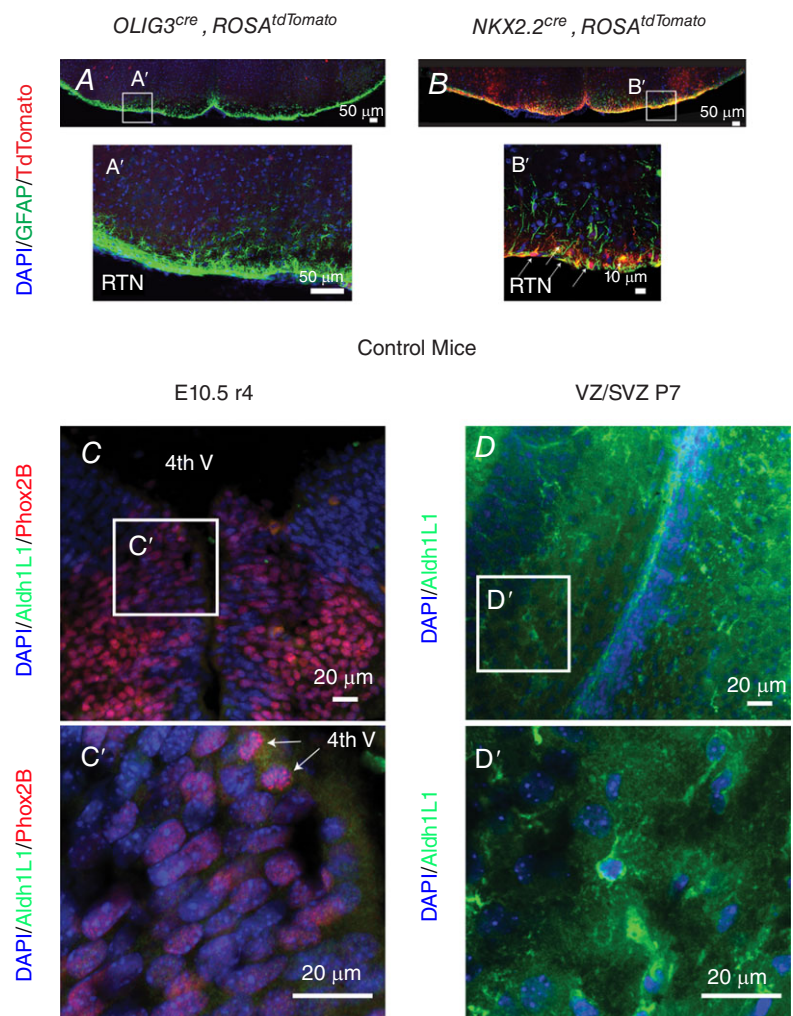


Figure 4. Mapping of glial populations

Genotypes displayed on the top, and colour-coded molecular markers on the left. *A*, sections of the ventral medulla at the RTN/pFRG level from *OLIG3^{cre}, ROSA^{tdTomato}* mice show no contribution to ventral medullary astrocytes. *B*, in contrast, the *NKX2.2^{cre}, ROSA^{tdTomato}* animals show robust contribution of astrocytes to the RTN/pFRG. *C*, coronal section of rhombomere 4 (r4) at E10.5 stained with *ALDH1L1* and *PHOX2B*. *C'*, inset showing that progenitors that ultimately give rise to ventral medullary *PHOX2B*-derived cells do not express *Aldh1L1* (image captured from the ventral neuroepithelium, spanning the pMNv domain. Note *PHOX2B* expression in mitotic cells (arrows). *D*, coronal section of VZ/SVZ stem cell populations that give rise to cortical neurons and glia. *D'*, inset showing positive controls for *ALDH1L1* immunostaining. [Colour figure can be viewed at wileyonlinelibrary.com]

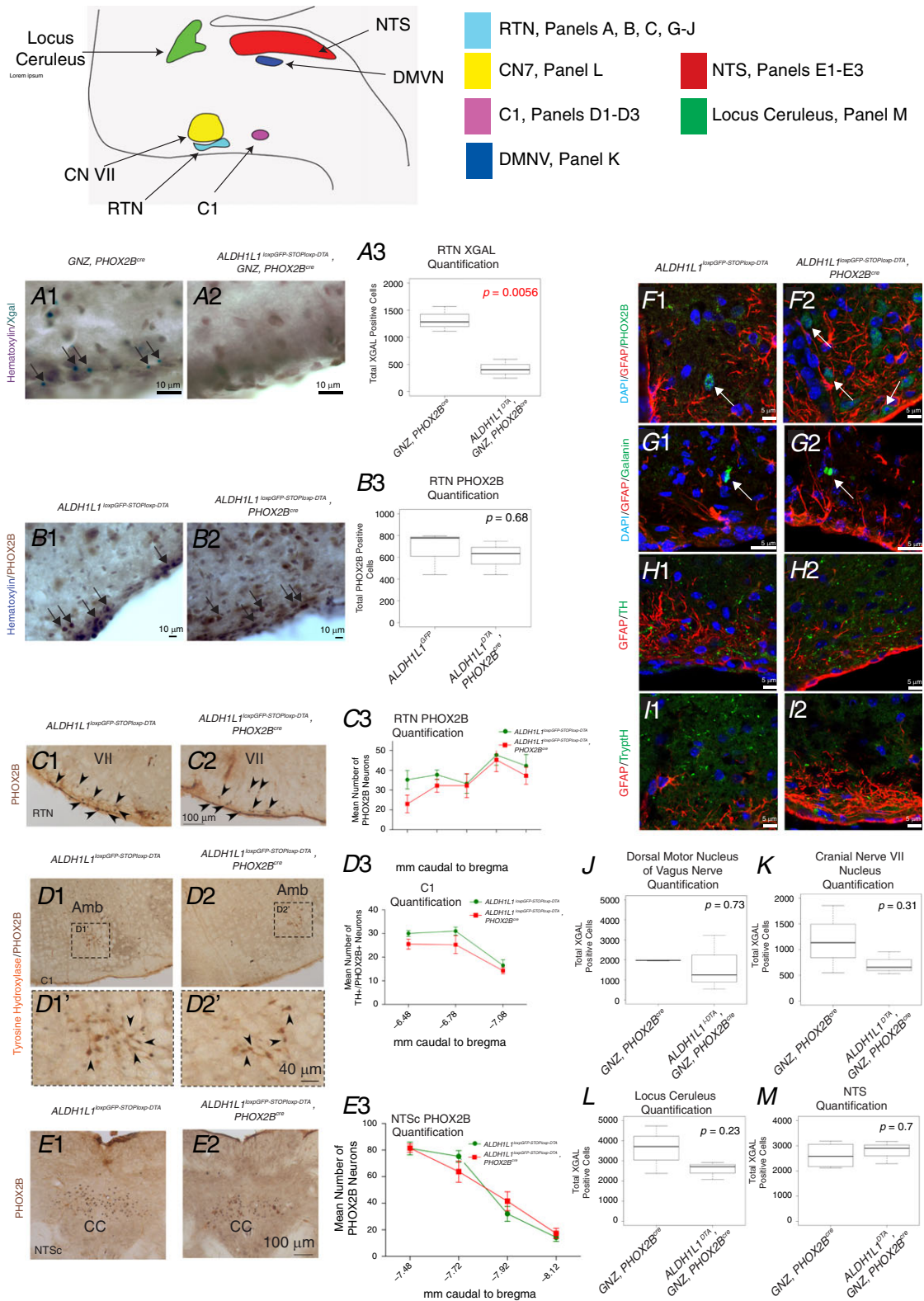


Figure 5. Ablation of PHOX2B-derived astrocytes results in cell loss only in the RTN/pFRG area of the ventral lateral medulla

A colour-coded schematic diagram of the different nuclei analysed is shown above the panels. RTN data is shown in panels A, B, C, F and I; CNVII data is shown in panel K; DMNV data is shown in panel J, NTS data is shown in panels E1–3, and M. Locus coeruleus is shown in panel L. Genotypes are denoted on top row, and molecular

known to be *PHOX2B*-derived (Fig. 5J–M). No significant difference existed in *PHOX2B*-derived cells in these regions, suggesting that *PHOX2B* progenitor cells do not significantly contribute glia to these structures. We conclude that ablation of *PHOX2B*-derived astrocytes is specific to the RTN, and further conclude that the number of *PHOX2B*-positive cells in the RTN, and commissural NTS were not reduced in *PHOX2B*-astrocyte-ablated animals.

Ablation of *PHOX2B*-derived astrocytes results in chemosensory impairment and moderate vigilance state fragmentation

Having verified that ablation of *PHOX2B*-derived, *ALDH1L1*-expressing cells does not affect development of *PHOX2B*-derived neurons, we tested the hypothesis that ablation of *PHOX2B*-derived astrocytes would result in chemosensory respiratory defects in mice. We first performed neurobehavioral analyses and found that *PHOX2B*-astrocyte ablation did not change anxiety (elevated plus maze test) or socialization behaviours (Fig. S2 in Supporting information). Having determined no changes in anxiety, we next set out to determine if *PHOX2B*-derived astrocyte ablation resulted in defects of chemosensory control. Negative control mice genotypes were *ALDH1L1^{loxP-GFP-STOP-loxP-DTA}*. Experimental astrocyte-ablated mouse genotypes were *PHOX2B^{cre}*, *ALDH1L1^{loxP-GFP-STOP-loxP-DTA}* (*PHOX2B*-derived astrocyte-ablated). We performed these experiments in postnatal day 1 (P1) pups, juvenile mice (P21) and adult mice. Juvenile or adult *PHOX2B*-derived astrocyte-ablated mice did not change baseline breathing (juvenile: V_T : 12 ± 0.5 vs. *ALDH1L1^{DTA}*: $11 \pm 0.3 \mu\text{l g}^{-1}$, $P = 0.2$; f_R : 252 ± 8.2 vs. *ALDH1L1^{DTA}*: 260 ± 8.9 breaths min^{-1} , $P = 0.5$; and \dot{V}_E : 3028 ± 93 vs. *ALDH1L1^{DTA}*: $2920 \pm 107 \mu\text{l min}^{-1} \text{g}^{-1}$, $P = 0.5$) and (adult: V_T : 13 ± 0.4 vs. *ALDH1L1^{DTA}*: $14 \pm 0.1 \mu\text{l g}^{-1}$, $P = 0.1$; f_R : 216 ± 12 vs. *ALDH1L1^{DTA}*: 212 ± 15 breaths min^{-1} , $P = 0.8$; and \dot{V}_E : 2854 ± 242 vs. *ALDH1L1^{DTA}*: $2971 \pm 218 \mu\text{l min}^{-1} \text{g}^{-1}$, $P = 0.7$) (Fig. 6A–D; H–J). We did not find a significant change in the baseline total respiratory cycle (T_{TOT}), inspiratory time (T_I) or expiratory time (T_E) between *PHOX2B^{cre}*, *ALDH1L1^{DTA}* and *ALDH1L1^{DTA}* (Fig. 6E–G; K–M).

Increases in breathing parameters elicited by hypercapnia (7% CO₂) were not different in *PHOX2B^{cre}*, *ALDH1L1^{DTA}* mice compared to the control *ALDH1L1^{DTA}* (Fig. 7). In contrast, adult *PHOX2B^{cre}*, *ALDH1L1^{DTA}* mice showed a significant decrease in HVR (8% O₂, balance N₂) (Fig. 7A–D). For example, the increases in V_T (14 ± 0.7 vs. *ALDH1L1^{DTA}*: $17 \pm 0.6 \mu\text{l g}^{-1}$, $P = 0.005$) and \dot{V}_E : 3101 ± 303 vs. *ALDH1L1^{DTA}*: $4247 \pm 280 \mu\text{l min}^{-1} \text{g}^{-1}$, $P = 0.04$) elicited by hypoxia were reduced in *PHOX2B^{cre}*, *ALDH1L1^{DTA}* conscious mice. No change in T_{TOT} , T_I or expiratory time T_E were noticed during hypoxia or hypercapnia between *PHOX2B^{cre}*, *ALDH1L1^{DTA}* and *ALDH1L1^{DTA}* mice (Fig. 6E–G; K–M and Fig. 7E–G; K–M). We also found no significant difference in HVR in newborn P1 pups (Fig. S4 in Supporting information). Temporal evaluation of the hypoxic phase demonstrated an intact acute/phase I, indicating that the carotid body function is presumably intact. However, we found a significant reduction in \dot{V}_E in the hypoxic ventilatory roll-off phase/phase II. These changes included reduced variability in breathing parameters during the roll-off phase in *PHOX2B*-ablated mice, as well as a more robust repression of ventilation during the roll-off phase in the *PHOX2B*-astrocyte-ablated mice (Fig. S3 in Supporting information). We therefore conclude that *PHOX2B*-derived astrocytes regulate the roll-off/phase II of the hypoxic response.

In order to inhibit the CO₂ response of the carotid bodies, we subjected the animals to hyperoxic hypercapnia, a physiological manoeuvre that inhibits the carotid body modulation of the chemoreflex (Souza *et al.* 2018). The experimental protocol is illustrated in Fig. 8A. We found no significant change in respiratory response during the hyperoxic hypercapnia challenge (Fig. 8B). However, in our cohort of *PHOX2B*-astrocyte-ablated mice, the recovery period following the hyperoxic hypercapnic challenge was quite different, and was characterized by an abnormal return to baseline. Specifically, f_R and \dot{V}_E increased while T_I and T_E decreased at the new baseline after recovery in the *PHOX2B*-astrocyte-ablated animals. These data may indicate that *PHOX2B*-astrocyte-ablated mice have an impaired ability to return to baseline following hyperoxic hypercapnic challenge.

It is a well-documented phenomenon that patients harbouring *PHOX2B* mutations display sleep disordered

marker evaluation is colour-coded on the left-hand side of each panel. In F–I, all cells show DAPI in blue to label nuclei. In panel A, Haematoxylin incubation was performed without the 'blueing' step so as to provide enhanced contrast between the aqua-green X-GAL reaction and nuclei. All X-GAL quantifications were performed on P21 mice. Quantifications of panels A3, B3, and J–M, show on the y-axis the total number of cells (bilaterally quantified in all structures by unbiased stereology). The box of the whisker plot represents the interquartile range, the black bar represents the median, the whiskers represent 1.5× the interquartile range, and the P value of a Student's *t* test is denoted in the top right corner of each box-whisker plot. Quantifications of panels C3, D3, and E3 show serial section quantifications (y-axis) relative to bregma (x-axis). Panels B and F are goat-anti-*PHOX2B*, whereas panels C–E are rabbit anti-*PHOX2B* antibody. Photomicrographs of structures quantified in panels J–M are shown in Fig. S1 in Supporting information. [Colour figure can be viewed at wileyonlinelibrary.com]

breathing (Weese-Mayer *et al.* 2010). Therefore, we sought to determine the extent to which ablation of PHOX2B-derived astrocytes affected sleep behaviours in these mice. These mice were first implanted with wireless EEG/EMG biotelemeters and allowed to recover

for 2 weeks. Next, we performed 2 days of baseline sleep analysis on both male and female mice. We recorded the amount of time spent in each vigilance state, number of bouts into each vigilance state, bout durations, as well as activity and transitions between

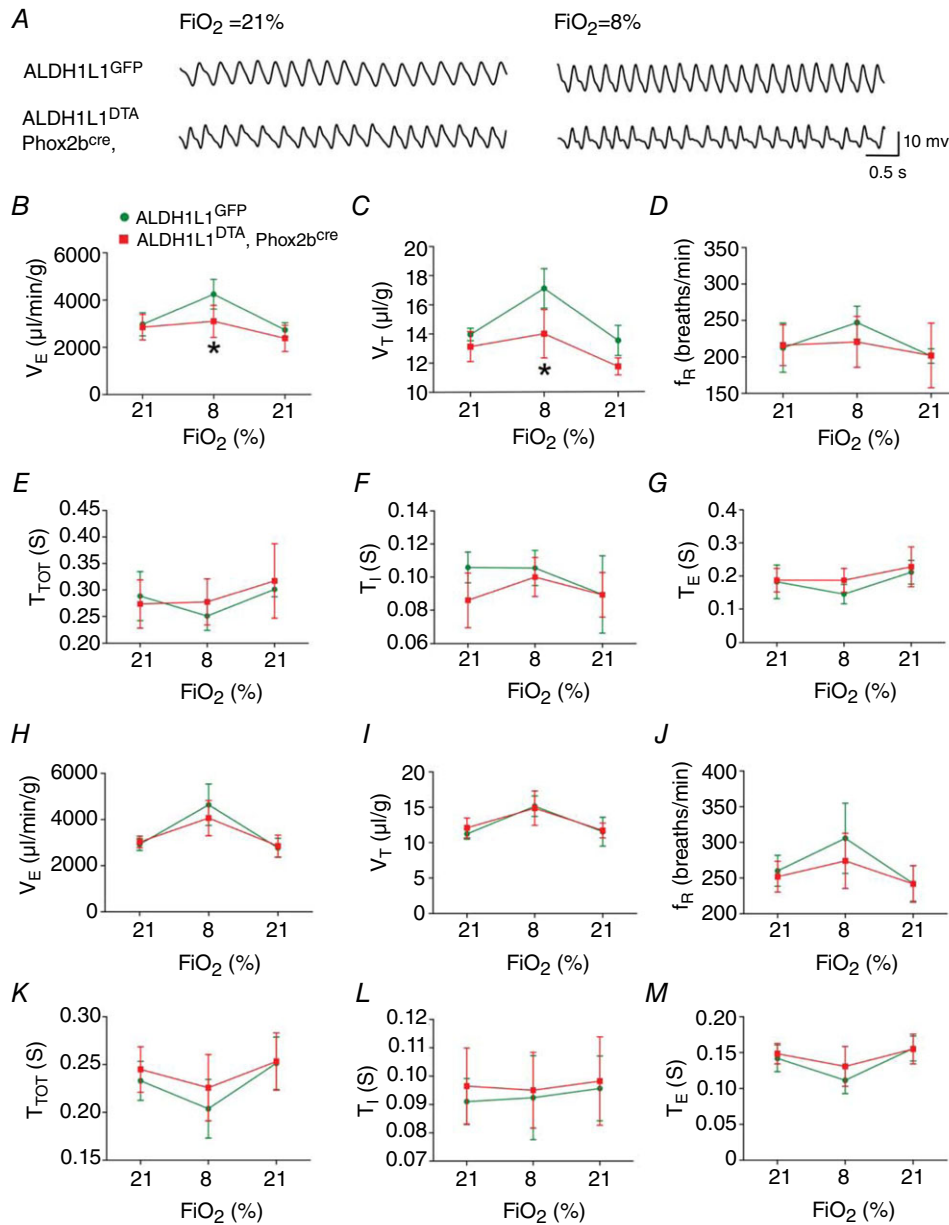


Figure 6. Hypoxic ventilatory response in juvenile and adult mice following PHOX2B-derived astrocyte ablation

A, recordings showing the effect of PHOX2B-derived astrocyte ablation under normoxia and hypoxia (8% O₂). B–G, changes in minute ventilation (\dot{V}_E , ml kg⁻¹ min⁻¹) (B), tidal volume (V_T , ml kg⁻¹) (C), respiratory frequency (f_R , breaths min⁻¹) (D), total respiratory cycle (T_{TOT} , s) (E), inspiratory time (T_I , s) (F) and expiratory time (T_E , s) (G) in adult conscious $ALDH1L1^{loxP-GFP-STOP-loxP-DTA}$ and $PHOX2B^{cre}$, $ALDH1L1^{loxP-GFP-STOP-loxP-DTA}$ mice under normoxia or hypoxic condition. H–M, changes in minute ventilation (\dot{V}_E , ml kg⁻¹ min⁻¹) (H), tidal volume (V_T , ml kg⁻¹) (I), respiratory frequency (f_R , breaths min⁻¹) (J), total respiratory cycle (T_{TOT} , s) (K), inspiratory time (T_I , s) (L) and expiratory time (T_E , s) (M) in juvenile conscious $ALDH1L1^{loxP-GFP-STOP-loxP-DTA}$ and $PHOX2B^{cre}$, $ALDH1L1^{loxP-GFP-STOP-loxP-DTA}$ mice under normoxia or hypoxic conditions. *Different from $ALDH1L1^{loxP-GFP-STOP-loxP-DTA}$ (control) (two-way ANOVA, $P < 0.05$); $n = 5$ /group of mice. [Colour figure can be viewed at wileyonlinelibrary.com]

each vigilance state. After attaining these baselines, we performed a 6-h ‘gentle handling’ sleep deprivation protocol, followed by an 18-h recovery period. During the first 6 h of recovery sleep, we also performed spectral analyses to ascertain the sleep quality. We noted that *PHOX2B*-derived astrocyte-ablated mice showed

increased spontaneous activity compared to control mice (Fig. S5 in Supporting information). No statistically significant differences in sleep timing or sleep amount was noted between groups (Fig. 9A–L). However, we noted that the *PHOX2B*-derived astrocyte-ablated mice increased the number of wake bouts and transitions between

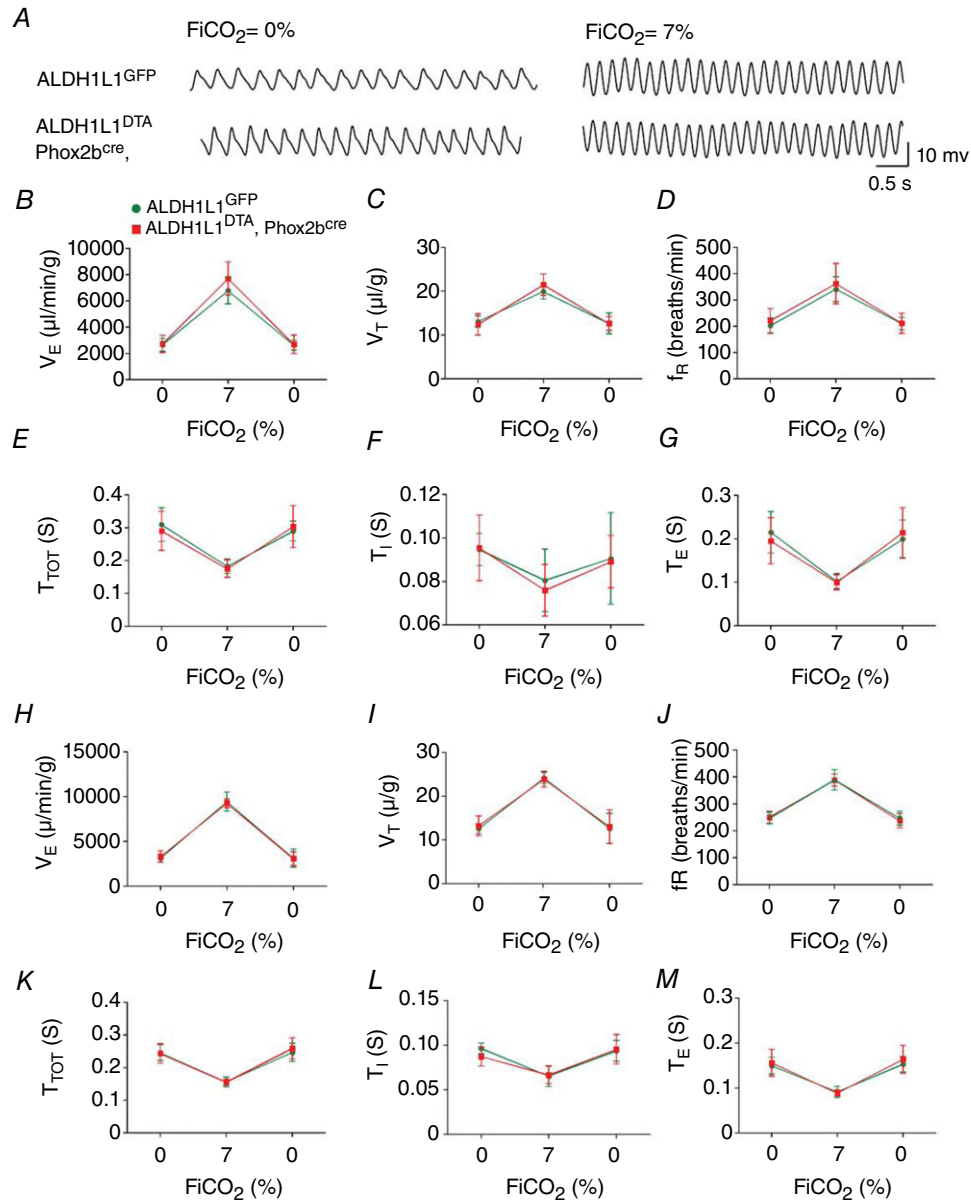


Figure 7. Hypercapnic ventilatory response in juvenile and adult mice following PHOX2B-derived astrocyte ablation
 A, recordings showing the effect of PHOX2B-derived astrocyte ablation under normocapnia and hypercapnia (7% CO₂). B–G, changes in minute ventilation (\dot{V}_E , ml kg⁻¹ min⁻¹) (B), tidal volume (V_T , ml kg⁻¹) (C), respiratory frequency (f_R , breaths min⁻¹) (D), total respiratory cycle (T_{TOT} , s) (E), inspiratory time (T_I , s) (F) and expiratory time (T_E , s) (G) in adult conscious *ALDH1L1^{loxP-GFP-STOP-loxP-DTA}* and *PHOX2B^{cre}*, *ALDH1L1^{loxP-GFP-STOP-loxP-DTA}* mice under normocapnia or hypercapnic condition. H–M, changes in minute ventilation (\dot{V}_E , ml kg⁻¹ min⁻¹) (H), tidal volume (V_T , ml kg⁻¹) (I), respiratory frequency (f_R , breaths min⁻¹) (J), total respiratory cycle (T_{TOT} , s) (K), inspiratory time (T_I , s) (L) and expiratory time (T_E , s) (M) in juvenile conscious *ALDH1L1^{loxP-GFP-STOP-loxP-DTA}* and *PHOX2B^{cre}*, *ALDH1L1^{loxP-GFP-STOP-loxP-DTA}* mice under normocapnia or hypercapnic condition. *Different from *ALDH1L1^{loxP-GFP-STOP-loxP-DTA}* (control) (two-way ANOVA, $P < 0.05$); $n = 6$ /group of mice. [Colour figure can be viewed at wileyonlinelibrary.com]

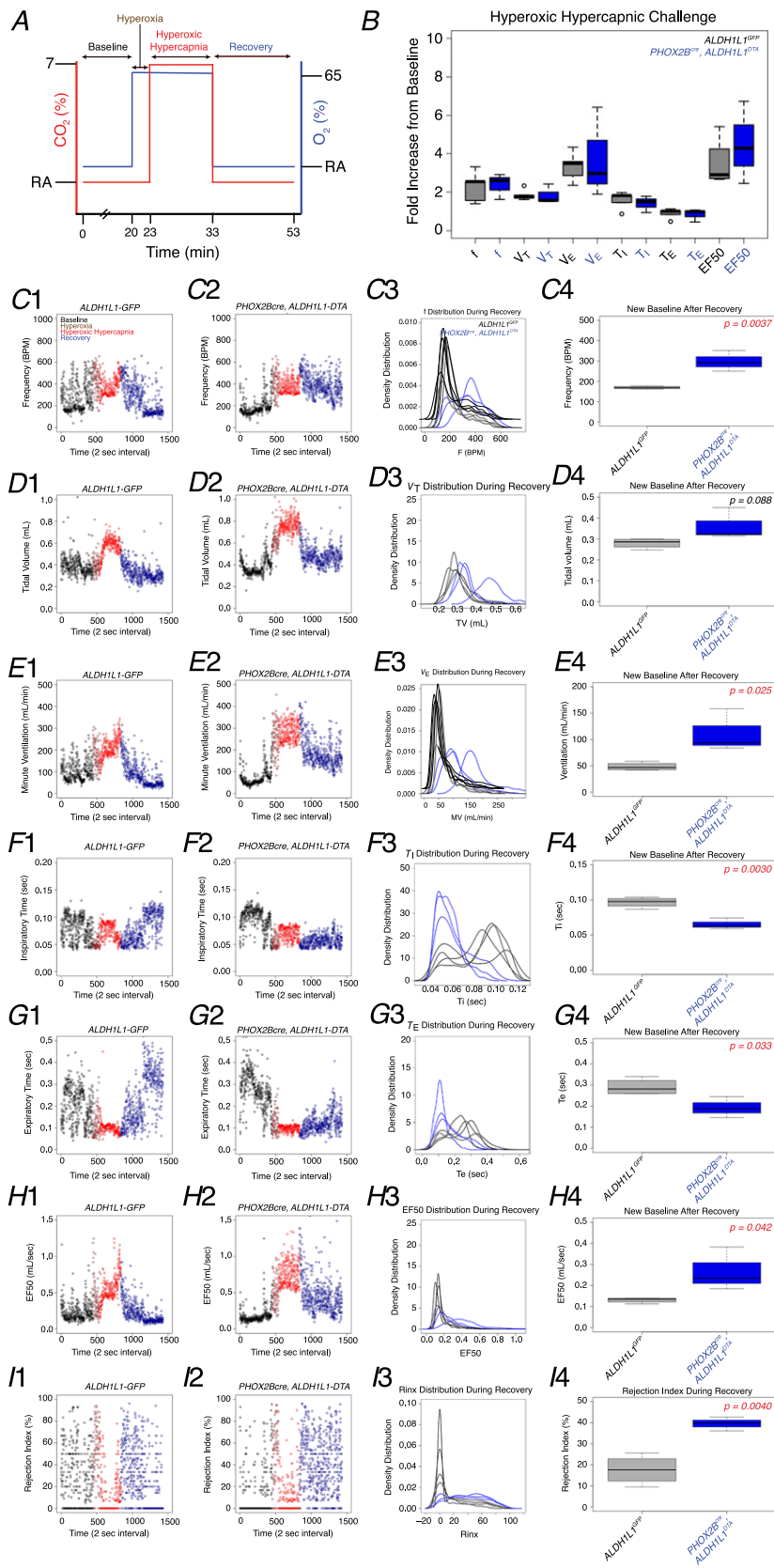


Figure 8. Defective recovery after hyperoxic hypercapnic challenge in mice following PHOX2B-derived astrocyte ablation

A, protocol for hyperoxic hypercapnic response. **B**, plot of response of hyperoxic-hypercapnic response. See Methods section for methodology. **C–I** show the defective respiratory pattern. Subpanels 1 and 2 in panels **C–H** represent the entire recording period, unfiltered, of two representative animals. As shown in the key of **C1**, baseline is black, hyperoxia is brown, hyperoxic hypercapnia is red, and recovery is in blue. Genotype is on top, and the parameter tested in on the bottom. Panels **C3**, **D3**, **E3**, **F3**, **G3**, and **I3** plot the best fit curve of the kernel density distribution. Genotypes are colour coded in the top of **C3**, with PHOX2B-derived astrocyte ablated animals shown in blue. The baseline measurements are plotted for each of the parameters in **C4**, **D4**, **E4**, **F4** and **G4**. **I4** shows the arithmetic mean of the rejection index during the recovery period. f , frequency; V_T , tidal volume; \dot{V}_E , minute ventilation; T_I , inspiratory time; T_E , expiratory time; EF50, mid expiratory flow. [Colour figure can be viewed at wileyonlinelibrary.com]

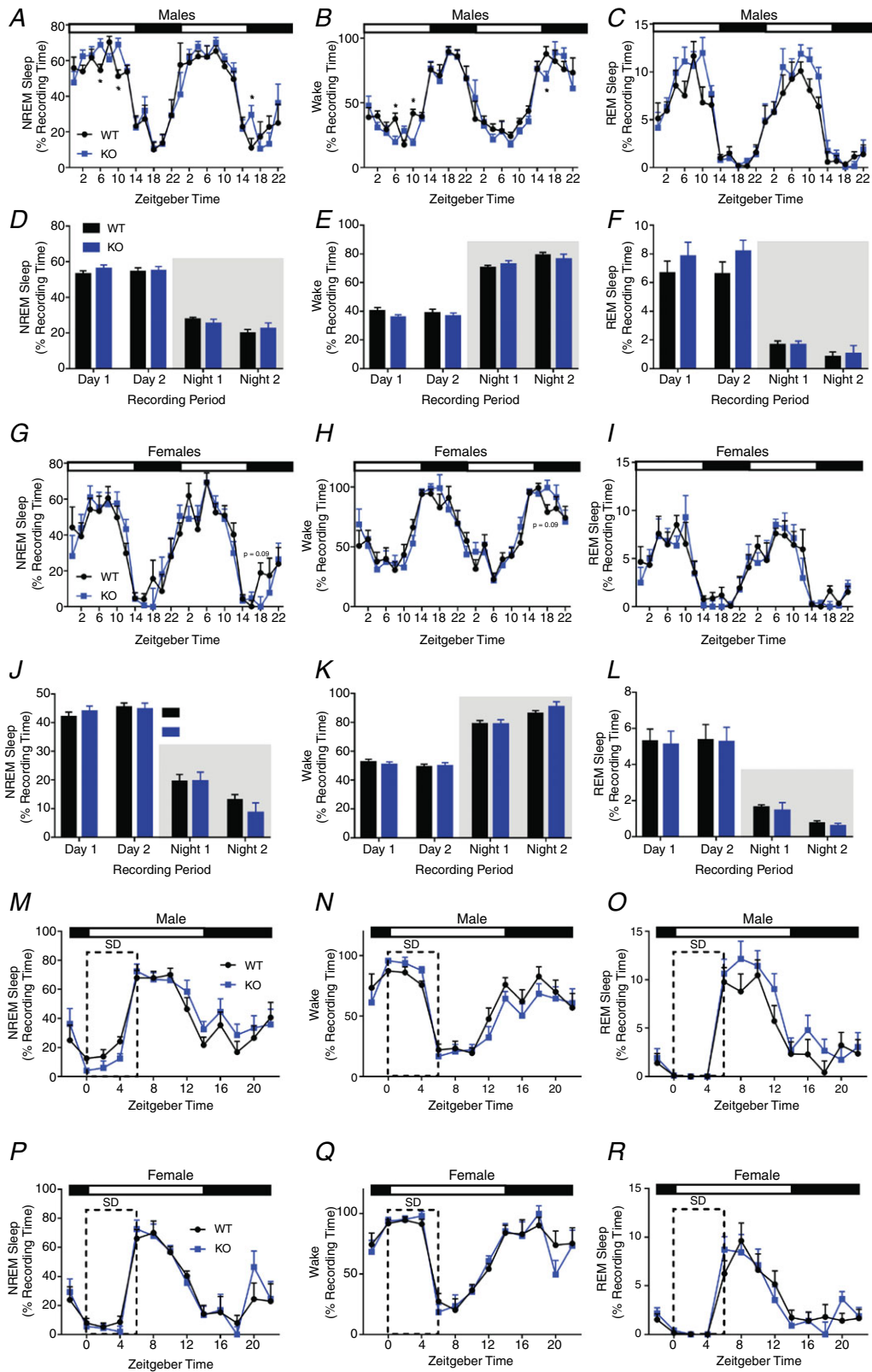


Figure 9. Sleep analysis in PHOX2B-astrocyte-ablated mice
 Percentage of time spent in each vigilance state is plotted for males (A–F) and females (G–L). PHOX2B-derived astrocyte ablation does not alter amount of time spent in NREM (A, G) wake (B, H), or REM sleep (C, I) in male (A–F) or female (G–L) mice. Error bars represent SEM, $n = 4/\text{sex/genotype}$, $*P < 0.05$ Student's t test. PHOX2B-derived

astrocyte ablation does not alter the normal REM or wake phases following sleep deprivation. Mice were sleep deprived (denoted by 'SD' in panels) via gentle handling for 6 h starting at 'lights on' (ZT 0), when sleep pressure was high. Male (*M-O*) and female (*P-R*) time spent (per 2 h bin) in each vigilance state during sleep deprivation and recovery was not different between genotypes. The spectral components of the EEG were analysed during 0–6 h following sleep deprivation (recovery sleep; ZT 6–12). Neither males (*C* and *D*) nor females (*G* and *H*) showed changes in the spectral components of wake or REM states during recovery sleep. Error bars represent SEM, $n = 4/\text{sex/genotype}$. [Colour figure can be viewed at wileyonlinelibrary.com]

vigilance states (Fig. 10A–F), suggesting fragmentation. Furthermore, the response to sleep deprivation was different amongst the genotypes (Fig. 10G–J). Although no changes in rebound sleep time were noted (Fig. 9M–R),

we observed that *PHOX2B*-derived astrocyte-ablated mice had decreased EEG delta power during baseline waking and that females showed an increase in delta power during sleep recovery (Fig. 10G–H), indicating higher

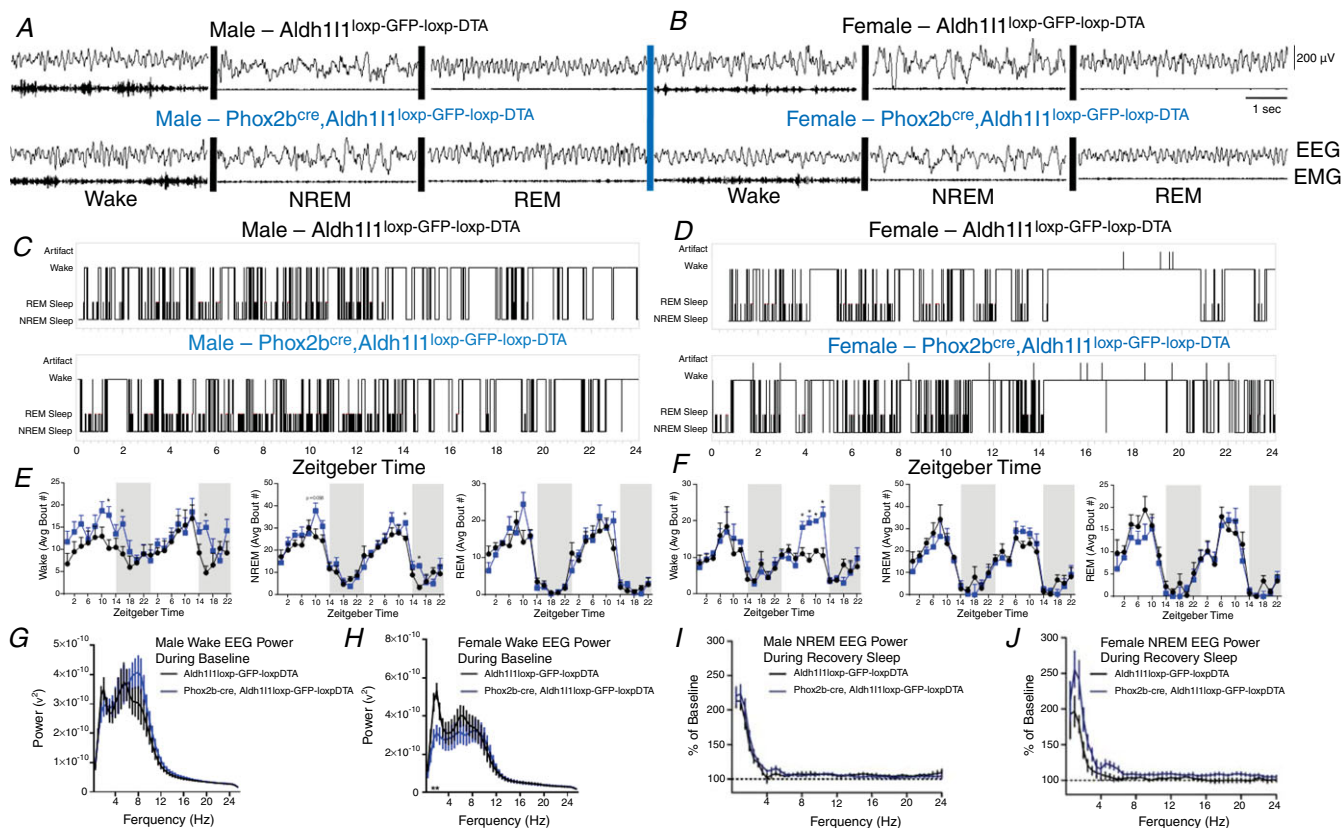


Figure 10. *PHOX2B*-derived astrocyte ablation results in moderate vigilance state fragmentation, reduced delta power during waking in female mice and increased delta power in females after sleep deprivation

A and *B*, representative 5 s EEG/EMG traces from male (*A*) and female (*B*) mice from each genotype. Each trace is accompanied by the corresponding vigilance state ('wake', 'NREM', or 'REM'). *C* and *D*, representative hypnograms of day 2 baseline recordings for male (*C*) and female (*D*) mice from each genotype. Notice that the mutants have more transitions between vigilance states. *E*, male *PHOX2B*-astrocyte ablated animals (blue line) demonstrate increased bout numbers in wakefulness (day 1: ZT 12 $t = 2.715$, $P = 0.035$; ZT 16 $t = 2.861$, $P = 0.023$; day 2: ZT 14 $t = 4.8$, $P = 0.003$) and NREM sleep (day 2: ZT 12 $t = 4.626$, $P = 0.0036$; ZT 16 $t = 6.302$, $P = 0.0007$). *F*, female *PHOX2B*-astrocyte ablated mice show more pronounced changes in wakefulness bouts (day 2: ZT 6 $t = 3.073$, $P = 0.02$; ZT 8 $t = 3.976$, $P = 0.007$; ZT 10 $t = 9.658$, $P = 0.00007$; ZT 12 $t = 3.754$, $P = 0.009$). *G* and *H*, no changes were observed in the spectral power (during all of baseline recording) of wake state in male mice (*G*), but we did observe altered wake spectral power in female *PHOX2B* astrocyte-ablated mice (*H*). Deletion of *PHOX2B*-derived astrocytes alters the homeostatic response to sleep deprivation in female mice. NREM spectral power during 0–6 h following sleep deprivation compared to baseline data collected at the same time on the previous day in male (*I*) and female (*J*) mice. Female mice lacking these astrocytes show enhanced delta (slow wave) power in response to a 6 h sleep deprivation protocol. Error bars represent SEM; $n = 4/\text{group/genotype}$. Frequencies 1.5 Hz, $t = 2.716$; $P = 0.035$; 2 Hz, $t = 3.573$, $P = 0.012$. Error bars represent SEM, $n = 4/\text{sex/genotype}$, $*P < 0.05$, Student's *t* test. [Colour figure can be viewed at wileyonlinelibrary.com]

perceived sleep pressure following sleep deprivation. We conclude that *PHOX2B*-derived astrocyte-ablated mice suffer moderate vigilance state fragmentation, increased activity, and altered EEG delta power during wakeful states and in response to total sleep deprivation.

***PHOX2B*-derived brainstem astrocytes are not significantly more chemosensitive than non-*PHOX2B*-derived brainstem astrocytes**

The aforementioned data demonstrate that *PHOX2B*-derived astrocytes show non-redundant functions with background astrocytes. We therefore set forth to identify the extent to which *PHOX2B*-derived astrocytes may show unique glial-sensory responses to either hypoxia or hypercapnia *in vitro*. To achieve this, we cultured brainstem astrocytes using a protocol to obtain a > 95% pure culture and performed calcium imaging experiments by loading the astrocytes with the calcium-sensitive dye Fluo-8. Fluctuations in intracellular calcium concentration are utilized as a proxy measure for astrocyte activation (Volterra *et al.* 2014). To identify *PHOX2B*-derived astrocytes, we extracted brainstems from *PHOX2B^{cre}*, *ROSA^{tdTomato}* mice, which showed *PHOX2B*-derived astrocytes in red (Fig. 11A and F). To determine the astrocyte response to hypoxia, we utilized two perfusate systems of artificial cerebrospinal fluid (aCSF): one equilibrated by bubbling in carbogen gas (95%O₂-5%CO₂) to represent normoxia, and hypoxic aCSF perfusate equilibrated with 100% N₂ gas (Fig. 11A and B). Representative examples of these videos are also shown in Supporting information (Videos S1–S10 in Supporting information). We note that many astrocytes showed an unexpected biphasic response to hypoxia. A typical response is plotted in Fig. 11B. Changing the baseline perfusate to the hypoxic perfusate causes an initial exponential increase in intracellular calcium, followed by a secondary linear phase. Returning the perfusate from hypoxia to normoxia caused a rapidly exponential return to baseline intracellular calcium levels. This response to hypoxia occurred in all cells, regardless of *PHOX2B* derivation, in a synchronized fashion (Videos S1–S4 in Supporting information). We next asked if these *PHOX2B*-derived astrocytes may play a role in hypoxia synchronization. To test this, we generated brainstem astrocyte cultures from control animals and *PHOX2B*-derived astrocyte-ablated animals (Fig. 11C–E). We performed image analysis on these videos so that we could identify, in an automated and unbiased fashion, cells that showed fluctuations in intracellular calcium (see Methods). Note that in both conditions, a massive globally synchronized change in intracellular calcium concentration occurs upon the initiation of hypoxia and on the re-institution of normoxia (see yellow rectangles

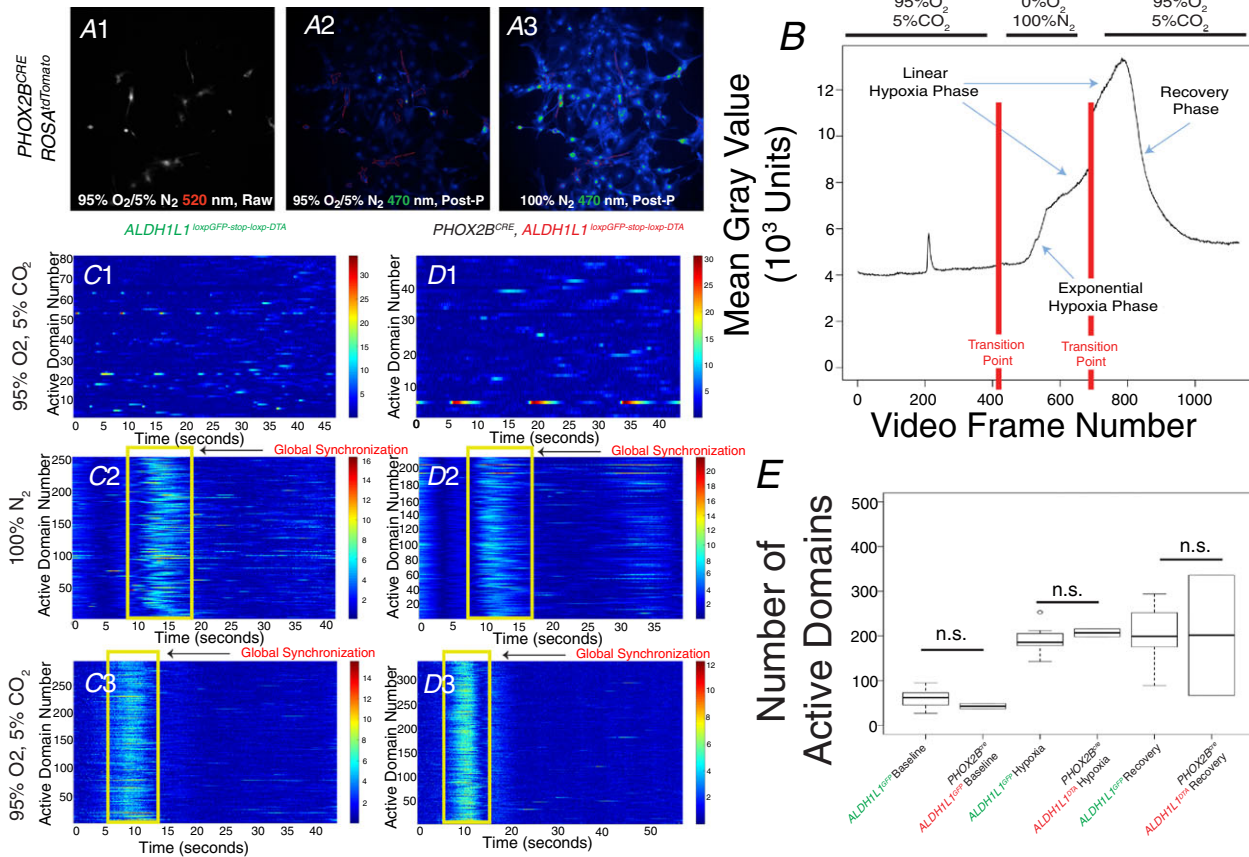
on the raster plots of Fig. 11C2, C3, D2 and D3). We conclude that *PHOX2B*-derived astrocytes are not required for globally synchronized astrocyte activation in response to hypoxia *in vitro*.

We performed parallel experiments to determine the extent to which *PHOX2B*-derived astrocytes were activated upon hypercapnia (Fig. 11F). Cells were loaded with the calcium-sensing dye Fluo-8, and imaged using time-lapse video epifluorescent microscopy as the cells were exposed to perfusates of artificial cerebrospinal fluid (aCSF) set to two pH settings: first baseline (pH 7.4) and then an acidification challenge (pH 7.2) (Fig. 9F–G). The response to acidification of these brainstem astrocytes was markedly different to the hypoxia response above. Representative examples of these videos are also shown in supplemental information (Videos S7–S10 in Supporting information). Many cells reacted to the acidification, but not necessarily by increasing activity. For instance, the cell plotted in Fig. 11G showed rhythmic fluctuations during baseline, which were abrogated following transition to the more acidic perfusate. Overall, we found that 20–50% of the cells showed increased bursting activity upon acidification with no difference identified between *PHOX2B*-derived and non-*PHOX2B*-derived astrocytes (Fig. 11H). We also did not identify significant synchronization of cell cultures of control of *PHOX2B*-astrocyte-depleted cultures (Fig. 11I–N). In summary, we were unable to find a difference in response to acidification between *PHOX2B*-derived and non-*PHOX2B*-derived astrocytes. We further conclude that the astrocyte response to acidification is, in general, heterogeneous, and that the aforementioned *in vivo* physiological defects elicited by ablating *PHOX2B*-derived astrocytes is probably not caused by a dysfunction of glial chemosensory responses to hypoxia or hypercapnia.

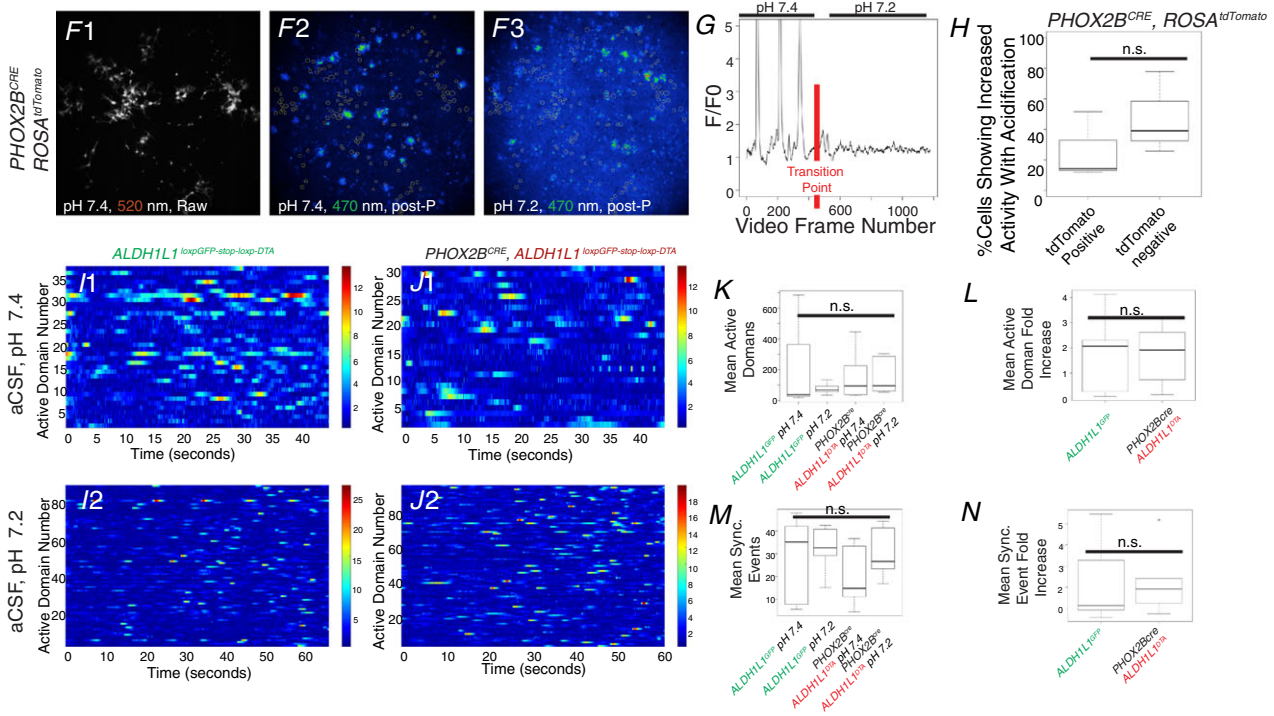
Ablation of *PHOX2B*-derived astrocytes results in neuronal dystrophy-like neuropathology in the RTN

The above data indicate that *PHOX2B*-derived astrocytes of the ventral lateral medulla modulate the second phase of the hypoxic ventilatory response, and that *PHOX2B*-derived astrocytes *do not* represent a chemosensitive-enriched astrocyte population. These data indicate that *PHOX2B*-derived astrocytes may regulate the chemosensory control of breathing through different mechanisms. Prior studies have shown astrocytes to be critical in synaptic integrity and circuit organization (Molofsky *et al.* 2014). Therefore, we tested if there were any ultrastructural cytoarchitectural findings that could mediate the physiological dysfunctions identified. To achieve this, we imaged the RTN region by electron microscopy to evaluate axon terminal morphology and

In vitro Astrocyte Hypoxia Challenge



In vitro Astrocyte Acidification Challenge



axon terminal organelles (Fig. 12). We noted that axon terminals in the mutants were on average larger in area and perimeter (Fig. 12*H* and *I*). Furthermore, we noted an increase in the percentage of axon terminals showing autophagic vacuoles/phagosomes (Fig. 12*A–D*, *G*). The proportion of axon terminals with other organelles, including mitochondria and dense core neurosecretory vesicles, was not different between groups (Fig. 12*P* and *Q*). These neuropathological findings are similar to those found in neuroaxonal dystrophies (Schmidt *et al.* 2008; Inoue *et al.* 2013), which are characterized by constant formation-degeneration-reformation of synapses. In summary, *PHOX2B*-derived, astrocyte ablated mice show synaptic pathology characterized by dysmorphic neuro-axonal morphology, suggesting an underlying defect in the afferent input into the RTN. These data suggest that *PHOX2B*-derived astrocytes may play a role in regulating the synaptic integrity of neuronal inputs into RTN neurons.

Discussion

Our data indicate that a subset of RTN astrocytes, derived from *PHOX2B*-positive progenitor cells, modulate the chemosensory control of breathing and furthermore are not redundant with other RTN astrocytes. These data align well with recent findings implicating astrocytes in the modulation of breathing circuits (Sheikhbahaei *et al.* 2018). The observation that *PHOX2B*-derived progenitor cells give rise to both astrocytes and neurons, albeit from different embryonic domains, indicates that physiologically relevant neuron-glia units show developmental relationships in the brainstem. Neurophysiological deficits occurring in adult animals that suffered embryonic

ablation of a small number of cells underscores the need for finely orchestrated integration of developing astrocytes with their neurons. Indeed, the notion of developmentally linked neuronal circuits is not new for *PHOX2B*-derived cells. Seminal discoveries over 20 years ago showing that *PHOX2B* expression could delineate physiologically linked afferent and efferent medullary pathways of neuronal autonomic circuits underscored that *PHOX2B* functions to not only pattern neural tube progenitor domains, but also instructs circuit patterning (Tiveron *et al.* 1996). Our data indicate that the principal of integrated *PHOX2B*-derived circuits also extend to astrocytes which play active roles in *PHOX2B*-dependent circuit functions. Manipulation of regional and sub-regional astrocytes and their genes, in combination with functional studies of neuron-glia interactions in specific networks, will bring novel insights into the ever evolving plethora of astrocyte roles in the neurophysiology.

Contribution of *PHOX2B*-derived astrocytes to breathing and medullary synaptic integrity

Astrocytes are sensitive to both pH (Gourine *et al.* 2010) and hypoxia (Angelova *et al.* 2015; Teschemacher *et al.* 2015; Turovsky *et al.* 2015). Our calcium imaging data demonstrate that hypoxia has a profound effect on astrocyte physiology, resulting in globally synchronized activity. In contrast, the response to acidification is heterogeneous, suggesting that different astrocytes are react to acidification differently. These primary chemosensory roles are redundant between *PHOX2B*-derived and non-*PHOX2B*-derived astrocytes. We propose that *PHOX2B*-derived astrocytes share principal functions related to the chemosensory control of breathing.

Figure 11. Chemosensory analysis of *PHOX2B*-derived astrocytes *in vitro*

In *A*, *PHOX2B*-derived astrocytes were identified by *tdTomato* expression (see genotype on left) identified by image capture of LED-illuminated samples (see wavelength on bottom left of panel). *A1* shows one image capture baseline live cells perfused with carbogen gas as a raw black and white image. *A2* and *A3* show Z-projection of summed activity during baseline carbogen recording or hypoxia recording, respectively. In *B*, we graph a common waveform identified in individual cells with mean grey value on the y-axis and video frame number on the x-axis (1 frame per 100 ms); red lines demonstrate transition points where movie recording was stopped to institute the different perfusate (indicated on top of graph). No differences were found between *PHOX2B*-derived astrocytes and non-*PHOX2B*-derived astrocytes. In panels *C–D*, brainstem astrocyte cultures derived from animals were analysed for global synchronization of the culture with the genotypes delineated on top, and perfusate condition delineated on the left (*D* denotes experiments with *PHOX2B*-derived astrocytes depleted from the culture.) In these raster plots, changes in fluorescence are shown by the blue-red colour spectrum (to the right of each graph), the x-axis shows time, and the y-axis is active domain number, which corresponds to cells that showed fluctuations in intracellular calcium. Note that during hypoxia (*C2* and *D2*), massive global synchronization is noted during hypoxia (yellow box) and an increase in active domains is detected during this recording period. In *C3* and *D3*, we also noted a massive global synchronization during the return to normoxia. We did not find a difference in the active domain numbers between these two genotypes. Similar experiments are performed in the *in vitro* astrocyte acidification, which constituted changing the perfusate from aCSF at pH 7.4, to aCSF at pH 7.2. In *G*, an example of a *PHOX2B*-derived astrocyte is plotted. In *H*, the percentage of astrocytes showing increased activity in response to acidification is plotted and shows no change between conditions. We also performed global synchronization experiments in *J–N*, and found no significant change in the fold increase in active domains (*K–L*) and no difference in the fold increase in synchronized events between conditions. Representative movies are shown in Videos S1–S10 in Supporting information. [Colour figure can be viewed at wileyonlinelibrary.com]

These astrocytes probably participate in the circuits regulating CNS-dependent secondary hypoxic ventilatory depression, complementing emerging evidence showing astrocytes participating in hypoxia effects on breathing (Angelova *et al.* 2015; Gourine & Funk, 2017). Purinergic signalling mechanisms have been attributed to these effects, since P2 receptor blockade in the ventrolateral medulla augments the hypoxia-induced secondary depression of ventilation in adult rats (Gourine *et al.* 2005). Our study focuses on the fact that the astrocyte regulated CNS hypoxic ventilatory response is also shared by *PHOX2B*-derived, RTN astrocytes in adult mice. Whether this specific population of astrocytes exerts its role through purinergic signalling in neurons is the subject of future investigation. Our work also demonstrates that the *PHOX2B*-derived neurons, which are involved in the central hypercarbic chemoreflex, do not require *PHOX2B*-derived astrocytes for proper hypercapnia ventilatory response.

In the present study, we propose that *PHOX2B*-derived astrocytes are critical for the maintenance of synaptic integrity. There is ample evidence showing that astrocytes

exert metabolic, structural and functional effects on neurons, reinforcing the notion that interactions between astrocytes and neurons are necessary to maintain CNS homeostasis (Benarroch, 2010; Chung *et al.* 2015a,b). The enlarged axonal terminal morphology with the increase in autophagic vacuoles/phagosomes of afferent terminals into the RTN region noted in *PHOX2B*-derived astrocyte-ablated mice is similar to that found in neuroaxonal dystrophies (Schmidt *et al.* 2008). Autophagic vacuoles are known to be formed in axon terminals and transported retrogradely to the neuronal somata for final degradation (Cheng *et al.* 2015). Neuroaxonal dystrophies ultimately result in neuronal degeneration and inefficient circuits (Yue *et al.* 2008). Indeed, some authors have proposed that elevation in neuronal autophagic vacuoles is indicative of nutrient-deprived conditions (Nikoletopoulou *et al.* 2015). Thus, dystrophic-like axonal terminal development may reflect lack of a supportive role that these astrocytes play in afferent pathways into the RTN, such as the hypoxic ventilatory response.

Classical studies describing the hypoxia ventilatory response were performed in the 19th century by Corneille

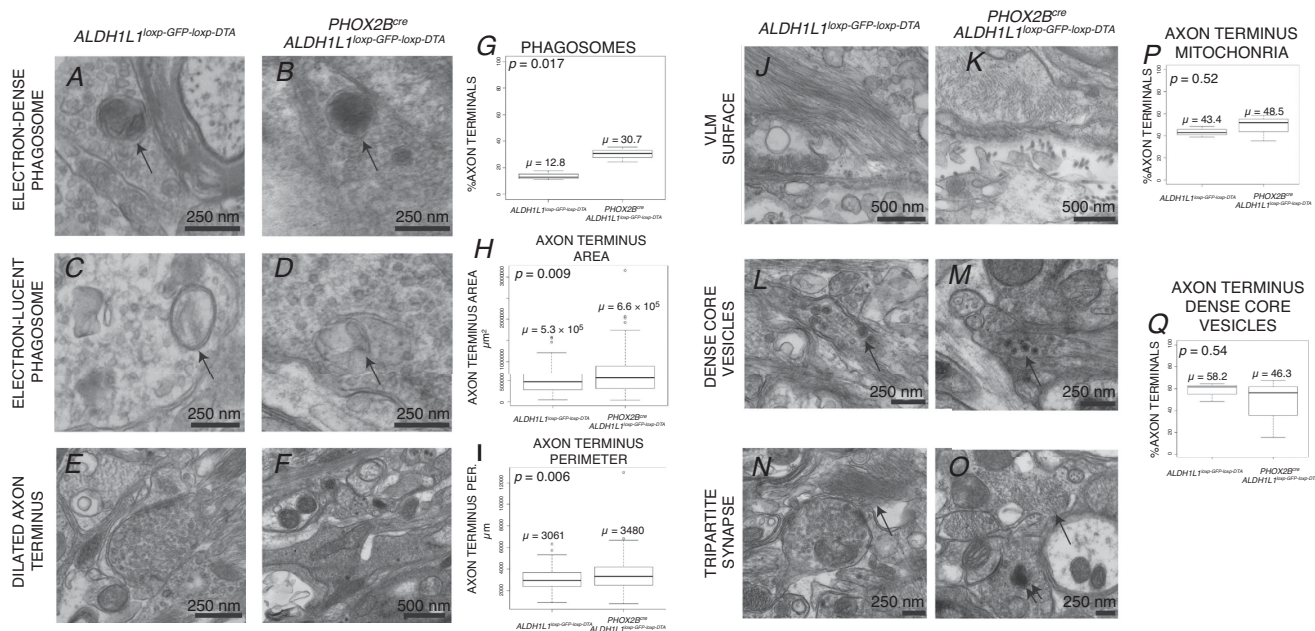


Figure 12. Ultrastructural analysis of RTN axon terminals

Images are delineated by theme on the left-hand side and by genotype on top. Phagosomes localized to RTN axon terminals were seen to be of two types illustrated in panels A–D (black arrow points to phagosome). Some phagosomes were large, membrane-bound vesicles with electron-dense material, whereas others were membrane-bound, electron-lucent vesicles. *PHOX2B^{cre}, Aldh11^{loxP-GFP-loxp-DTA}* showed a propensity to having larger axon terminals than controls (E and F). G, axon terminal phagosome quantification. H, axon terminus area plot. I, axon terminus perimeter plot. Ultrastructural morphology of the ventral lateral surface in control and *PHOX2B*-derived astrocyte-ablated animals shows no change between groups, with intermediate filament rich astrocyte foot processes extending to the pial surface and pial-arachnoidal fibroblast-like cells depositing collagen. Abundant dense core neurosecretory granules were found in axon terminals in both groups (N–O, quantified in K). We did not see differences in tripartite synapses (Q and R). In the box plots in panels G, H, I, J and K, continuous lines within the box denote population median, box denotes the interquartile range, and the whiskers denote 1.5 × the interquartile range. The P-statistic in top left of panels G, H, I, J and K is derived from Student's t test. μ, mean.

Heymans (for review see Prabhakar & Semenza, 2015). Low levels of O_2 stimulate carotid body glomus cells which then activate second order neurons in the nucleus of the solitary tract (NTS). The NTS then directly activates the respiratory central pattern generator (rCPG) and the rCPG ultimately drives the breathing output (Guyenet, 2014). A second mechanism relies on the existence of a central respiratory oxygen sensor, potentially mediated by brainstem astrocytes (Angelova *et al.* 2015; Gourine & Funk, 2017). In this scenario, RTN astrocytes would be able to sense a decrease in brain parenchyma P_{O_2} and trigger several biological cascades such as mitochondrial depolarization and activation of phospholipase C and IP3, which induce release of Ca^{2+} and enhanced ATP release (Huxtable *et al.* 2010). Although it is possible that PHOX2B-derived astrocytes could mediate the O_2 chemosensory response, our findings of dysmorphic axon terminals in the RTN region raise the possibility that the O_2 chemosensory response requires PHOX2B-derived astrocytes for efficient activation of the rCPG but does not require them to be the primary sensor of blood P_{O_2} . We note that disynaptic inputs which relay input from the NTS to the rCPG via RTN chemoreceptor neurons are strongly activated by peripheral chemoreceptor stimulation to provide powerful excitatory input to the rCPG (Takakura *et al.* 2006).

State-dependent control by PHOX2B-derived astrocytes

Our data show more transitions between NREM, REM and wake states in animals lacking Phox2B-derived astrocytes. Specifically, both males and females display more wake bouts during the light cycle and females also show more bouts of NREM during the dark cycle. Thus, although the amount of time spent in each state was unchanged, the structure of the sleep was distinct in the PHOX2B-astrocyte-ablated animals. Furthermore, despite the finding that the amount of time the animals slept in response to sleep deprivation was unchanged, changes in NREM delta power were observed during the sleep deprivation recovery. NREM delta power is inversely related to prior sleep debt. These results indicate that PHOX2B astrocyte-ablated mice enhanced NREM delta power responses to sleep deprivation, showing that they build more sleep pressure during an equal time of prior wakefulness. These findings are in-line with our fragmentation data, where moderate changes in sleep-wake stability (i.e. fragmentation) do not allow these mice to get 'good, deep sleep (NREM delta dominated)'. The mice must then make up for this deficit during recovery sleep in an attempt to restore sleep homeostasis. These data provide evidence that PHOX2b astrocyte ablation fragments sleep (without changing the total amount; which is a phenotype observed in debilitating

sleep disorders such as narcolepsy; Khatami *et al.* 2007; Yun *et al.* 2017), affecting sleep quality in response to sleep deprivation.

These phenomena could be explained by two general hypotheses. The first is that the presence of PHOX2B-derived astrocytes is crucial to maintaining the proper function of circuits projecting from the brainstem to sleep control centres in the basal forebrain. Monoaminergic systems in the brain exert different physiological and behavioural modulatory influences on their widespread targets. These effects are related primarily to central regulation of autonomic functions, motor activity, and the sleep-wake-arousal cycle (Jouvet, 1972; Astonjones & Bloom, 1981; Jacobs *et al.* 1990). Following this rationale, a dysfunction in these circuits precipitated by the lack of PHOX2B-derived astrocytes would result in sleep-wake cycle disturbances. These sleep problems may or may not be caused by the existing chemosensation defect. Evidence in the literature suggests that increases in CO_2 can lead to arousal in humans in the absence of changes in respiratory mechanoreceptor activity (Ayas *et al.* 2000). This observation could be the result of locus coeruleus noradrenaline-containing neurons sending parallel signals into both the medullary respiratory network for adjustment of ventilatory drive and the CNS structures responsible for arousal. Indeed, the activity of noradrenergic neurons in the locus coeruleus has an important role in the sleep-wake cycle. They discharge selectively during wakefulness and become silent during sleep (Hobson *et al.* 1975; Astonjones & Bloom, 1981). If PHOX2B-derived astrocytes are important in maintaining these proper firing patterns, then their absence could lead to alterations of sleep-wake patterns.

Alternatively, the sleep phenotype of these mice could be attributed to a decrease in adenosine levels resulting from the absence of PHOX2B-derived astrocytes. Indeed, adenosine increases sleep drive by modulating the activity of several neuron types in important sleep control areas, including the mesopontine tegmentum (Rainnie *et al.* 1994; Arrigoni *et al.* 2001), hypothalamus (Chamberlin *et al.* 2003; Morairty *et al.* 2004; Gallopin *et al.* 2005; Methippara *et al.* 2005; Liu & Gao, 2007) and basal forebrain (Alam *et al.* 1999; Thakkar *et al.* 2003). Astrocytes play a major part in the production of extracellular adenosine by secretion of ATP and have been shown to modulate sleep recovery of an animal after sleep deprivation (Halassa *et al.* 2009). This phenomenon could serve to explain the changes in wake spectral power exhibited by female mutants, perhaps indicating a role for this astrocyte population in female sleep drive. Adenosine-mediated modulation of sleep drive could occur independently from the chemosensation phenotype and serve to amplify the already present effect of neuronal dysfunction due to the absence of PHOX2B-derived astrocytes.

References

- Agarwal A, Wu PH, Hughes EG, Fukaya M, Tischfield MA, Langseth AJ, Wirtz D & Bergles DE (2017). Transient opening of the mitochondrial permeability transition pore induces microdomain calcium transients in astrocyte processes. *Neuron* **93**, 587–605.e7.
- Alam MN, Szymusiak R, Gong H, King J & McGinty D (1999). Adenosinergic modulation of rat basal forebrain neurons during sleep and waking: neuronal recording with microdialysis. *J Physiol* **521**, 679–690.
- Amiel J, Laudier B, Attie-Bitach T, Trang H, de Pontual L, Gener B, Trochet D, Etchevers H, Ray P, Simonneau M, Vekemans M, Munnich A, Gaultier C & Lyonnet S (2003). Polyalanine expansion and frameshift mutations of the paired-like homeobox gene PHOX2B in congenital central hypoventilation syndrome. *Nat Genet* **33**, 459–461.
- Angelova PR, Kasymov V, Christie I, Sheikhabaei S, Turovsky E, Marina N, Korsak A, Zwicker J, Teschemacher AG, Ackland GL, Funk GD, Kasparov S, Abramov AY & Gourine AV (2015). Functional oxygen sensitivity of astrocytes. *J Neurosci* **35**, 10460–10473.
- Arrigoni E, Rainnie DG, McCarley RW & Greene RW (2001). Adenosine-mediated presynaptic modulation of glutamatergic transmission in the laterodorsal tegmentum. *J Neurosci* **21**, 1076–1085.
- Astonjones G & Bloom FE (1981). Activity of norepinephrine-containing locus coeruleus neurons in behaving rats anticipates fluctuations in the sleep-waking cycle. *J Neurosci* **1**, 876–886.
- Ayas NT, Brown R & Shea SA (2000). Hypercapnia can induce arousal from sleep in the absence of altered respiratory mechanoreception. *Am J Respir Crit Care Med* **162**, 1004–1008.
- Bartlett D & Tenney SM (1970). Control of breathing in experimental anemia. *Respir Physiol* **10**, 384–395.
- Benarroch EE (2010). Glycogen metabolism: metabolic coupling between astrocytes and neurons. *Neurology* **74**, 919–923.
- Borniger JC, Walker Ii WH, Surbhi, Emmer KM, Zhang N, Zalenski AA, Muscarella SL, Fitzgerald JA, Smith AN, Braam CJ, TinKai T, Magalang UJ, Lustberg MB, Nelson RJ & DeVries AC (2018). A role for hypocretin/orexin in metabolic and sleep abnormalities in a mouse model of non-metastatic breast cancer. *Cell Metab* **28**, 118–129.e5.
- Brunet JF & Pattyn A (2002). Phox2 genes – from patterning to connectivity. *Curr Opin Genet Dev* **12**, 435–440.
- Bushong EA, Martone ME, Jones YZ & Ellisman MH (2002). Protoplasmic astrocytes in CA1 stratum radiatum occupy separate anatomical domains. *J Neurosci* **22**, 183–192.
- Chamberlin NL, Arrigoni E, Chou TC, Scammell TE, Greene RW & Saper CB (2003). Effects of adenosine on gabaergic synaptic inputs to identified ventrolateral preoptic neurons. *Neuroscience* **119**, 913–918.
- Cheng XT, Zhou B, Lin MY, Cai Q & Sheng ZH (2015). Axonal autophagosomes recruit dynein for retrograde transport through fusion with late endosomes. *J Cell Biol* **209**, 377–386.
- Chung WS, Allen NJ & Eroglu C (2015a). Astrocytes control synapse formation, function, and elimination. *Cold Spring Harb Perspect Biol* **7**, a020370.
- Chung WS, Welsh CA, Barres BA & Stevens B (2015b). Do glia drive synaptic and cognitive impairment in disease? *Nat Neurosci* **18**, 1539–1545.
- Dauger S, Pattyn A, Lofaso F, Gaultier C, Goridis C, Gallego J & Brunet JF (2003). Phox2b controls the development of peripheral chemoreceptors and afferent visceral pathways. *Development* **130**, 6635–6642.
- Dubreuil V, Hirsch MR, Pattyn A, Brunet JF & Goridis C (2000). The Phox2b transcription factor coordinately regulates neuronal cell cycle exit and identity. *Development* **127**, 5191–5201.
- Gallopin T, Luppi PH, Cauli B, Urade Y, Rossier J, Hayaishi O, Lambolez B & Fort P (2005). The endogenous somnogen adenosine excites a subset of sleep-promoting neurons via A_{2A} receptors in the ventrolateral preoptic nucleus. *Neuroscience* **134**, 1377–1390.
- Gokozan HN, Baig F, Corcoran S, Catacutan FP, Gygli PE, Takakura AC, Moreira TS, Czeisler C & Otero JJ (2016). Area postrema undergoes dynamic postnatal changes in mice and humans. *J Comp Neurol* **524**, 1259–1269.
- Gourine AV & Funk GD (2017). On the existence of a central respiratory oxygen sensor. *J Appl Physiol (1985)* **123**, 1344–1349.
- Gourine AV, Kasymov V, Marina N, Tang F, Figueiredo MF, Lane S, Teschemacher AG, Spyer KM, Deisseroth K & Kasparov S (2010). Astrocytes control breathing through pH-dependent release of ATP. *Science* **329**, 571–575.
- Gourine AV, Llaudet E, Dale N & Spyer KM (2005). ATP is a mediator of chemosensory transduction in the central nervous system. *Nature* **436**, 108–111.
- Guyenet PG (2014). Regulation of breathing and autonomic outflows by chemoreceptors. *Compr Physiol* **4**, 1511–1562.
- Gygli PE, Chang JC, Gokozan HN, Catacutan FP, Schmidt TA, Kaya B, Goksel M, Baig FS, Chen S, Griveau A, Michowski W, Wong M, Palanichamy K, Sicinski P, Nelson RJ, Czeisler C & Otero JJ (2016). Cyclin A2 promotes DNA repair in the brain during both development and aging. *Aging* **8**, 1540–1570.
- Halassa MM, Florian C, Fellin T, Munoz JR, Lee SY, Abel T, Haydon PG & Frank MG (2009). Astrocytic modulation of sleep homeostasis and cognitive consequences of sleep loss. *Neuron* **61**, 213–219.
- Hazai D, Szudoczki R, Ding J, Soderling SH, Weinberg RJ, Sotonyi P & Racz B (2013). Ultrastructural abnormalities in CA1 hippocampus caused by deletion of the actin regulator WAVE-1. *PLoS One* **8**, e75248.
- Hirsch MR, d'Autreaux F, Dymecki SM, Brunet JF & Goridis C (2013). A Phox2b::FLPo transgenic mouse line suitable for intersectional genetics. *Genesis* **51**, 506–514.
- Hobson JA, Mccarley RW & Wyzinski PW (1975). Sleep cycle oscillation – reciprocal discharge by 2 brain-stem neuronal groups. *Science* **189**, 55–58.
- Huxtable AG, Zwicker JD, Alvares TS, Ruangkittisakul A, Fang X, Hahn LB, Posse de Chaves E, Baker GB, Ballanyi K & Funk GD (2010). Glia contribute to the purinergic modulation of inspiratory rhythm-generating networks. *J Neurosci* **30**, 3947–3958.

- Inoue K, Rispoli J, Yang L, Macleod D, Beal MF, Klann E & Abeliovich A (2013). Coordinate regulation of mature dopaminergic axon morphology by macroautophagy and the PTEN signaling pathway. *PLoS Genet* **9**, e1003845.
- Jacobs BL, Fornal CA & Wilkinson LO (1990). Neurophysiological and neurochemical studies of brain serotonergic neurons in behaving animals. *Ann NY Acad Sci* **600**, 260–271.
- Jouvet M (1972). Role of monoamines and acetylcholine-containing neurons in regulation of sleep-waking cycle. *Erg Physiol Biol Ch* **64**, 166–307.
- Khatami R, Landolt HP, Achermann P, Retey JV, Werth E, Mathis J & Bassetti CL (2007). Insufficient non-REM sleep intensity in narcolepsy-cataplexy. *Sleep* **30**, 980–989.
- Liu ZW & Gao XB (2007). Adenosine inhibits activity of hypocretin/orexin neurons by the A1 receptor in the lateral hypothalamus: A possible sleep-promoting effect. *J Neurophysiol* **97**, 837–848.
- Malan A (1973). Ventilation measured by body plethysmography in hibernating mammals and in poikilotherms. *Respir Physiol* **17**, 32–44.
- Marina N, Abdala AP, Trapp S, Li A, Nattie EE, Hewinson J, Smith JC, Paton JF & Gourine AV (2010). Essential role of Phox2b-expressing ventrolateral brainstem neurons in the chemosensory control of inspiration and expiration. *J Neurosci* **30**, 12466–12473.
- Methippara MM, Kumar S, Alam MN, Szymusiak R & McGinty D (2005). Effects on sleep of microdialysis of adenosine A1 and A2a receptor analogs into the lateral preoptic area of rats. *Am J Physiol Regul Integr Comp Physiol* **289**, R1715–R1723.
- Molofsky AV, Kelley KW, Tsai HH, Redmond SA, Chang SM, Madireddy L, Chan JR, Baranzini SE, Ullian EM & Rowitch DH (2014). Astrocyte-encoded positional cues maintain sensorimotor circuit integrity. *Nature* **509**, 189–194.
- Morairty S, Rainnie D, McCarley R & Greene R (2004). Disinhibition of ventrolateral preoptic area sleep-active neurons by adenosine: a new mechanism for sleep promotion. *Neuroscience* **123**, 451–457.
- Nikoletopoulou V, Papatheou ME & Tavernarakis N (2015). Autophagy in the physiology and pathology of the central nervous system. *Cell Death Differ* **22**, 398–407.
- Nobuta H, Cilio MR, Danhaive O, Tsai HH, Tupal S, Chang SM, Murnen A, Kreitzer F, Bravo V, Czeisler C, Gokozan HN, Gygli P, Bush S, Weese-Mayer DE, Conklin B, Yee SP, Huang EJ, Gray PA, Rowitch D & Otero JJ (2015). Dysregulation of locus coeruleus development in congenital central hypoventilation syndrome. *Acta Neuropathol* **130**, 171–183.
- Ogata K & Kosaka T (2002). Structural and quantitative analysis of astrocytes in the mouse hippocampus. *Neuroscience* **113**, 221–233.
- Ostergaard PJ & Jensen MB (2013). Histological quantification of astrocytosis after cerebral infarction: a systematic review. *Int J Neurosci* **123**, 439–443.
- Otero JJ, Fu W, Kan L, Cuadra AE & Kessler JA (2004a). Beta-catenin signaling is required for neural differentiation of embryonic stem cells. *Development* **131**, 3545–3557.
- Otero JJ, Fu W, Kan L, Cuadra AE & Kessler JA (2004b). Beta-Catenin signaling is required for neural differentiation of embryonic stem cells. *Development* **131**, 3545–3557.
- Otero JJ, Kalaszczynska I, Michowski W, Wong M, Gygli PE, Gokozan HN, Griveau A, Odajima J, Czeisler C, Catacutan FP, Murnen A, Schuller U, Scinski P & Rowitch D (2014). Cerebellar cortical lamination and foliation require cyclin A2. *Dev Biol* **385**, 328–339.
- Oyanedel CN, Kelemen E., Scheller J, Rose-John S (2015). Peripheral and central blockade of interleukin-6 trans-signaling differentially affects sleep architecture. *Brain Behav Immun* **50**, 178–185.
- Panman L, Andersson E, Alekseenko Z, Hedlund E, Kee N, Mong J, Uhde CW, Deng Q, Sandberg R, Stanton LW, Ericson J & Perlmann T (2011). Transcription factor-induced lineage selection of stem-cell-derived neural progenitor cells. *Cell Stem Cell* **8**, 663–675.
- Pattyn A, Goridis C & Brunet JF (2000a). Specification of the central noradrenergic phenotype by the homeobox gene Phox2b. *Mol Cell Neurosci* **15**, 235–243.
- Pattyn A, Hirsch M, Goridis C & Brunet JF (2000b). Control of hindbrain motor neuron differentiation by the homeobox gene Phox2b. *Development* **127**, 1349–1358.
- Pattyn A, Morin X, Cremer H, Goridis C & Brunet JF (1997). Expression and interactions of the two closely related homeobox genes Phox2a and Phox2b during neurogenesis. *Development* **124**, 4065–4075.
- Pattyn A, Vallstedt A, Dias JM, Samad OA, Krumlauf R, Rijli FM, Brunet JF & Ericson J (2003). Coordinated temporal and spatial control of motor neuron and serotonergic neuron generation from a common pool of CNS progenitors. *Genes Dev* **17**, 729–737.
- Peretz Y, Eren N, Kohl A, Hen G, Yaniv K, Weisinger K, Cinnamon Y & Sela-Donenfeld D (2016). A new role of hindbrain boundaries as pools of neural stem/progenitor cells regulated by Sox2. *BMC Biol* **14**, 57.
- Prabhakar NR & Semenza GL (2015). Oxygen sensing and homeostasis. *Physiology (Bethesda)* **30**, 340–348.
- Rainnie DG, Grunze HCR, McCarley RW & Greene RW (1994). Adenosine inhibition of mesopontine cholinergic neurons – implications for EEG arousal. *Science* **263**, 689–692.
- Ramanantsoa N, Hirsch MR, Thoby-Brisson M, Dubreuil V, Bouvier J, Ruffault PL, Matrot B, Fortin G, Brunet JF, Gallego J & Goridis C (2011). Breathing without CO₂ chemosensitivity in conditional Phox2b mutants. *J Neurosci* **31**, 12880–12888.
- Ruffault PL, D'Autreaux F, Hayes JA, Nomaksteinsky M, Autran S, Fujiyama T, Hoshino M, Hagglund M, Kiehn O, Brunet JF, Fortin G & Goridis C (2015). The retrotrapezoid nucleus neurons expressing Atoh1 and Phox2b are essential for the respiratory response to CO₂. *eLife* **4**, e07051.
- Schmidt RE, Parvin CA & Green KG (2008). Synaptic ultrastructural alterations anticipate the development of neuroaxonal dystrophy in sympathetic ganglia of aged and diabetic mice. *J Neuropathol Exp Neurol* **67**, 1166–1186.
- Sheikhabaei S, Morris B, Collina J, Anjum S, Znati S, Gamarra J, Zhang R, Gourine AV & Smith JC (2018). Morphometric analysis of astrocytes in brainstem respiratory regions. *J Comp Neurol* **526**, 2032–2047.

- Souza G, Kanbar R, Stornetta DS, Abbott SGB, Stornetta RL & Guyenet PG (2018). Breathing regulation and blood gas homeostasis after near complete lesions of the retrotrapezoid nucleus in adult rats. *J Physiol* **596**, 2521–2545.
- Stornetta RL, Moreira TS, Takakura AC, Kang BJ, Chang DA, West GH, Brunet JF, Mulkey DK, Bayliss DA & Guyenet PG (2006). Expression of Phox2b by brainstem neurons involved in chemosensory integration in the adult rat. *J Neurosci* **26**, 10305–10314.
- Takakura AC, Barna BF, Cruz JC, Colombari E & Moreira TS (2014). Phox2b-expressing retrotrapezoid neurons and the integration of central and peripheral chemosensory control of breathing in conscious rats. *Exp Physiol* **99**, 571–585.
- Takakura AC, Moreira TS, Colombari E, West GH, Stornetta RL & Guyenet PG (2006). Peripheral chemoreceptor inputs to retrotrapezoid nucleus (RTN) CO₂-sensitive neurons in rats. *J Physiol* **572**, 503–523.
- Takakura AC, Moreira TS, Stornetta RL, West GH, Gwilt JM & Guyenet PG (2008). Selective lesion of retrotrapezoid Phox2b-expressing neurons raises the apnoeic threshold in rats. *J Physiol* **586**, 2975–2991.
- Teschemacher AG, Gourine AV & Kasparov S (2015). A role for astrocytes in sensing the brain microenvironment and neuro-metabolic integration. *Neurochem Res* **40**, 2386–2393.
- Thakkar MM, Delgiacco RA, Strecker RE & McCarley RW (2003). Adenosinergic inhibition of basal forebrain wakefulness-active neurons: A simultaneous unit recording and microdialysis study in freely behaving cats. *Neuroscience* **122**, 1107–1113.
- Tiveron MC, Hirsch MR & Brunet JF (1996). The expression pattern of the transcription factor Phox2 delineates synaptic pathways of the autonomic nervous system. *J Neurosci* **16**, 7649–7660.
- Tsai HH, Li H, Fuentealba LC, Molofsky AV, Taveira-Marques R, Zhuang H, Tenney A, Murnen AT, Fancy SP, Merkle F, Kessaris N, Alvarez-Buylla A, Richardson WD & Rowitch DH (2012). Regional astrocyte allocation regulates CNS synaptogenesis and repair. *Science* **337**, 358–362.
- Turovsky E, Karagiannis A, Abdala AP & Gourine AV (2015). Impaired CO sensitivity of astrocytes in a mouse model of Rett syndrome. *J Physiol* **593**, 3159–3168.
- Volterra A, Liaudet N & Savtchouk I (2014). Astrocyte Ca²⁺ signalling: an unexpected complexity. *Nat Rev Neurosci* **15**, 327–335.
- Weese-Mayer DE & Berry-Kravis EM (2004). Genetics of congenital central hypoventilation syndrome: lessons from a seemingly orphan disease. *Am J Respir Crit Care Med* **170**, 16–21.
- Weese-Mayer DE, Berry-Kravis EM, Ceccherini I, Keens TG, Loghmanee DA & Trang H (2010). An official ATS clinical policy statement: Congenital central hypoventilation syndrome: genetic basis, diagnosis, and management. *Am J Respir Crit Care Med* **181**, 626–644.
- Yue Z, Wang QJ & Komatsu M (2008). Neuronal autophagy: going the distance to the axon. *Autophagy* **4**, 94–96.
- Yun SH, Choi HD & Seo WS (2017). Spectral analysis of polysomnography in narcolepsy. *Psychiatry Investig* **14**, 193–197.

Additional information

Competing interests

The authors have no competing conflicts of interests.

Author contributions

CMC, TMS, ST, YW, RJN, JR, ACT, TSM, JJO conceived and designed the paper. CMC, TMS, SRF, JL, BK, AC, SM, PES, ARB, MG, JCB, NZ, SAFJ, FC, MJA, RJN, VS, ACT, TSM and JJO contributed to acquisition. CMC, TMS, YW, JCB, SAFJ, MJA, RJN, ACT, TSM and JJO analysed data. CMC, TMS, ST, YW, JCB, SAFJ, MJA, RJN, ACT, TSM and JJO interpreted the data. CMC, TMS, YW, JCB, RJN, ACT, TSM and JJO drafted the paper. All authors have approved the final version of the manuscript and agree to be accountable for all aspects of the work. All persons designated as authors qualify for authorship, and all those who qualify for authorship are listed.

Funding

This work was supported by NIH/NHLBI (R01HL132355 for C.M.C., J.J.O.), NIH/NINDS (P30 NS045758, R.N.). This research was also supported by public funding from São Paulo Research Foundation (FAPESP) (Grants: 2016/23281-3 to A.C.T.; 2015/23376-1 and 2016/22069-0 to T.S.M.). T.M.S. acknowledges 2017/12678-2 funding from FAPESP.

Acknowledgements

The authors would like to thank Dr Eric Huang for fruitful discussion.

Supporting information

Additional supporting information may be found online in the Supporting Information section at the end of the article.

Figure S1. Histological analysis of PHOX2B-astrocyte ablated mice.

Figure S2. PHOX2B-derived astrocyte ablated mice do not show significant increases in anxiety behavior compared to controls.

Figure S3. Chemoreflex analysis in Adult PHOX2B-astrocyte ablated mice.

Figure S4. Hypoxic chemoreflex in newborn pups.

Figure S5. PHOX2B-derived astrocyte ablation increases spontaneous locomotor activity.

Video S1. Representative video of brainstem astrocyte response to hypoxia experiment. This video shows the raw video during baseline.

Video S2. Representative video of brainstem astrocyte response to hypoxia experiment. This video shows the raw video during baseline following stack subtraction obtained from our imaging workflow pseudocolored in LUT.

Video S3. Representative video of brainstem astrocyte response to hypoxia experiment. This video shows the raw video during hypoxia.

Video S4. Representative video of brainstem astrocyte response to hypoxia experiment. This video shows the raw video during hypoxia following stack subtraction obtained from our imaging workflow pseudocolored in LUT.

Video S5. Representative video of brainstem astrocyte response to hypoxia experiment. This video shows the raw video during recovery to normoxia.

Video S6. Representative video of brainstem astrocyte response to hypoxia experiment. This video shows the raw video during recovery to normoxia following stack subtraction obtained from our imaging workflow pseudocolored in LUT.

Video S7. Representative video of brainstem astrocyte response to hypercapnia experiment. This video shows the raw video during baseline, aCSF at pH 7.4.

Video S8. Representative video of brainstem astrocyte response to hypoxia experiment. This video shows the raw video during baseline, aCSF at pH 7.4, following stack subtraction obtained from our imaging workflow pseudocolored in LUT.

Video S9. Representative video of brainstem astrocyte response to hypercapnia experiment. This video shows the raw video during acidification, aCSF at pH 7.2.

Video S10. Representative video of brainstem astrocyte response to hypercapnia experiment. This video shows the raw video during acidification, aCSF at pH 7.2, following stack subtraction obtained from our imaging workflow pseudocolored in LUT.